1-1-2012

3-D Fibrous Network of TiO2 Nanoparticles: Raman Sensor Development

Dmitry Maznichenko
Ryerson University

3-D FIBROUS NETWORK OF TiO_2 NANOPARTICLES: RAMAN SENSOR DEVELOPMENT

by

Dmitry Maznichenko

Bachelor of Engineering, Ryerson University, 2010

A thesis presented to Ryerson University

in partial fulfillment of the

requirements for the degree of

Master of Applied Science

in the Program of

Mechanical Engineering

Toronto, Ontario, Canada, 2012

AUTHOR'S DECLARATION

I hereby declare that I am the sole author of this thesis. This is a true copy of the thesis, including any required final revisions, as accepted by my examiners.

I authorize Ryerson University to lend this thesis to other institutions or individuals for the purpose of scholarly research

I further authorize Ryerson University to reproduce this thesis by photocopying or by other means, in total or in part, at the request of other institutions or individuals for the purpose of scholarly research.

I understand that my thesis may be made electronically available to the public.

ABSTRACT

3-D Fibrous Network of TiO_2 Nanoparticles: Raman Sensor Development

Bachelor of Engineering, 2010

Dmitry Maznichenko

Master of Applied Science, Mechanical Engineering

Ryerson University

A 3-D nano-fiber particle network of TiO_2 nanoparticles is synthesized by pulsed femtosecond laser irradiation of a pure Ti substrate. This study investigated the properties of the resulting nanostructure for chemical and biomolecular detection by Raman spectroscopy. Controlled tuning of surface roughness, porosity and depth of the 3-D network were found to directly influence Raman detection. The presented findings support a previously unrealized detection capacity by TiO_2. Crystal violet was used to test the Surface-Enhanced Raman Spectroscopy (SERS) performance of the developed TiO_2 sensor pads. The corresponding Raman enhancement factor was determined to be $1.3x10^6$ which is directly comparable to commercial Ag and Au based Raman substrates. Bisphenol-A and diclofenac sodium salt were introduced into drinking water and tested with various sensor pads to develop a Raman detection map. The results suggest an affinity towards uniform TiO_2 3-D nanofibrous networks.

ACKNOWLEDGEMENTS

Dr. Krishnan Venkatakrishnan and Dr. Tan Bo have provided me with invaluable support in guiding my research. I am thankful for their guidance and trust. I also thank Dr. Selvaganapathy for collaboration on evaluating the merit of chemical behavior on the prepared nanomodified substrates and Dr. Venkat Venkataramanan at the Institute for Optical Sciences at University of Toronto for providing the use of his Raman spectroscopy machine.

TABLE OF CONTENTS

Page

Author's Declaration ii

Abstract iii

Acknowledgements iv

Table of Contents v

Glossary viii

List of Tables ix

List of Figures x

List of Appendices xiii

CHAPTER 1: INTRODUCTION TO TITANIUM DIOXIDE

1.1 Metallurgy 2

1.2 Nanostructure Synthesis 3

1.3 Previous Lab Group Studies 6

1.4 Molecular Sensing 7

1.5 Research Objective 12

CHAPTER 2: RAMAN SPECTROSCOPY OF TITANIUM DIOXIDE

2.1 Plasmonics 13

2.2 Characterising Spectroscopic Peaks 14

2.3 Rutile Phase 15

2.4 Anatase Phase 18

CHAPTER 3: EXPERIMENTAL MATERIALS AND METHODS

3.1 Femtosecond Pulsed Laser 20

3.2 Materials 22

3.3 Surface Characterization 23

CHAPTER 4: NANOFIBROUS 3-D NETWORK

4.1 Plume Characteristics 26

4.2 Nanofibers 27

4.3 Substrate Effects 33

4.4 Summary 34

CHAPTER 5: NANOFIBROUS SERS EFFECT

5.1 Raman Analysis 35

5.2 EM Enhancement Mechanisms 37

5.3 Summary 43

CHAPTER 6: RAMAN MOLECULAR DETECTION

6.1 Crystal Violet Dye 44

6.2 Bisphenol-A 46

6.3 Diclofenac Sodium Salt 47

6.4 Raman Detection Map 48

CHAPTER 6: RAMAN MOLECULAR DETECTION

6.5 Summary 52

CHAPTER 7: CONCLUSION AND RECOMMENDATIONS 53

APPENDICES A1

REFERENCE LIST A22

CV A37

GLOSSARY

AFM	atomic force microscopy
BPA	bisphenol A
DSS	diclofenac sodium salt
EDX	energy dispersive x-ray spectroscopy
EM	electromagnetic
LSPR	localized surface plasmon resonance
NPs	nanoparticles
SEM	scanning electron microscopy
SERS	surface enhanced Raman spectroscopy
SNOM	scanning near-field microspcopy
TEM	transmission electron microscopy
UV	ultraviolet
XRD	x-ray diffraction
I_L	incident laser beam intensity (W/cm^2)
f	laser repetition rate (MHz)
Max	maximum surface roughness (V)
P	average femtosecond laser power (W)
P_{RS}	power of Raman scattered energy (W)
S_a	surface roughness (V)
t	laser dwell time (sec)
σ^R	Raman scattering cross section (cm^{-2})
ω_o	theoretical spot size diameter (μm)
ω_p	plasma resonance frequency (MHz)

LIST OF TABLES

TABLE	DESCRIPTION	PAGE
2.1	Observed spectrum and associated vibrational modes of rutile	17
2.2	Observed spectrum and associated vibrational modes of anatase	19
A.1.1	List of inorganic parameters present in Toronto drinking	A1
A.4.1	TiO_2 nanowires compared to the present study nanofibers	A13
A.4.2	CV to TiO_2 adsorption equilibrium from UV-vis spectrophotometer measure…	A14
A.4.3	Sources of error when calculating the analytical Raman EF	A15

LIST OF FIGURES

FIGURE	DESCRIPTION	PAGE
1.1	TiO_2 structural polymorphs[3]	2
1.2	TiO_2 nanoparticle synthesis review	3
1.3	TEM scans of high-purity nanotubes at optimum conditions[6]	4
1.4	Porous anodic alumina (left) used as a template for titania nanotubes (right)[8]	5
1.5	Electrospinning process of TiO_2, SEM scan inset[10]	6
1.6	Cyclic voltammogram showing quasi-reversible redox signal of ferrocyanide on SnO_2 as diffused through the semi-conducting TiO_2 mesoporous film[17]	8
1.7	Light interaction with a surface	9
1.8	Epithelial cell DNA mapping using the 1000 cm^{-1} wavenumber for CARS[20]	10
2.2	Variations in energy shifts determining activity for CO_2 [37]	14
2.3	Lattice vibrations of rutile [39]	15
2.4	Raman spectroscopy of rutile, the 521 cm^{-1} peak results from the Si substrate[40]	17
2.5	Lattice vibrations of anatase[1]	18
2.6	Raman spectroscopy of anatase, the 521 cm^{-1} peak results from the Si sub.[40]	19
4.1	TiO_2 nanofibrous network synthesis towards favorable SERS interface	21
6.1	Summary of nanofiber generation and coverage for 26 MHz and 13 MHz laser pulse repetition rates and varying durations	25
6.2	Laser ablation plasma evolution[56]	27
6.3	Initiation of TiO_2 nano-fiber formation	28
6.4	TiO_2 nanofibrous porosity development	29
6.5	EDX analysis of TiO_2 nanofibers	29

6.6 Raman spectra demonstrating synthesis parameter-variable TiO_2 30

6.7 AFM (left side) and corresponding SEM (right side) for low density (top row) and high density (bottom row) nanofibers..... 32

6.8 Thermal effects on the Ti substrate from femtosecond laser irradiation 33

6.9 Micro-via AFM scans for various 3-D networks..... 34

8.1 LSPR valence electron oscillation by a spherical model[63] 35

8.2 Raman spectra of three chosen substrates synthesized..... 36

8.3 A model of the SERS nanofibrous network mechanisms..... 38

8.4 TEM of segregated TiO_2 nanofibers..... 40

8.5 Plasmonic hybridization demonstrated [88] 41

10.1 CV-TiO_2 Raman spectra enhancement using a 26 MHz -15 msec substrate..... 45

10.2 Detection of aqueous (aq.) and dry residue (dr.) BPA by various sensor pads 46

10.3 Detection of dry residue DSS by various sensor pads. 48

10.4 Raman detection sensitivity map averaged for all TiO_2 sensor pad experiments.... 49

10.5 Roughness parameter G vs. Max reflection intensity 51

A.1.1 Raman signal under aqueous conditions dominated by background noise when using a commercial Ti substrate A2

A.2.2 Micro-via contribution to Raman signal A3

A.2.3 SNOM reflection map for different sensor pads.....A5

A.3.1 Degradation summary of the CV dye A6

A.3.2 CV-TiO_2 experiments using the 8 MHz -15msec substrate.....A7

A.3.3 CV-TiO_2 experiments using the 13 MHz -15msec substrate..... A8

A.3.4 CV-TiO_2 experiments using the 8 MHz -1msec substrate A9

A.3.5 Highest observed enhancement of the CV dye A10

A.3.6 CV-TiO_2 experiments using the 26 MHz -15msec substrate A11

A.5.1 Representation of G roughness construct A16

A.5.2 Limits of Raman detection correlated with SNOM experiments A17

A.5.3 Identified SNOM data outliers A18

A.5.4 Multiple-pulse femtosecond laser fluence characteristics A19

A.6.1 AFM cross-sectional view A20

LIST OF APPENDICES

APPENDIX	DESCRIPTION	PAGE
A.1	Drinking Water Analysis	A1
A.2	Raman, AFM and SNOM data	A2
A.3	Complete Crystal Violet Dye Experiments	A6
A.4	Raman Enhancement Factor Calculation	A12
A.5	Determining the Best Raman Sensor Pad	A16
A.6	Cross-Section Analysis	A19

CHAPTER 1

INTRODUCTION TO TITANIUM DIOXIDE

Nano-technology has been emerging with great potential for commercial and industrial applications. By definition, the nominal size of nanostructures range from 1 - 100 nm. The excitement originates from new material properties observed when bulk materials are reduced to the nanoscale. In this study, titanium (Ti) was chosen for its popular anti-corrosion and strength properties in bulk. When oxidized, TiO_2 acts as a semi-conductor with good thermal stability and biocompatibility properties. TiO_2 nanoparticles also effectively reflect ultraviolet (UV) radiation and are in current commercial production for skin sunblock. Additionally, TiO_2 can accept electron injection from photo-excited sensitizer molecular states and hence are widely investigated for solar applications. TiO_2 may likewise also promote redox reactions and effectively photodegenerate environmental pollutants under UV radiation.

However, Ag and in particular Au nanoparticles are dominant amongst chemical and biosensor applications. Their immediate electrical properties are favorable for many commercial electrochemistry, chromatography and photonic sensing applications. The presented findings will investigate the use of TiO_2 nanofibrous 3-D network for Raman scattering spectroscopy as a viable chemical and biomolecular sensor.

Many different nano-synthesis routes are currently available. They will be briefly examined and compared to the synthesis method of this thesis—femtosecond pulsed laser irradiation. It will be shown that every synthesis route tends to yield unique nano-structures that promote Raman scattering activity.

1.1 METALLURGY

Titanium dioxide is derived from ilmenite ores and mined from rutile beach sand. There are three naturally occurring crystalline modifications of TiO_2: rutile, anatase and brookite.[1] The most stable phase is anatase for particle sizes smaller than 40 nm and rutile for larger particle sizes. rutile is a stable form of TiO_2 when temperature exceeds 750 ^oC.[2] On the other hand, brookite is difficult to obtain under any condition and hence studies have been limited. In these investigations, neither EDX diffraction patterns nor Raman spectrum indicated it was present in the 3-D nanofiber particle network hence brookite will be omitted from further review.

The basic crystal structure of TiO_2 is composed of two unit cells. The Ti atoms are placed at the corners of the cell while the O atoms are in the middle. Variations between phases are due to the variation in TiO_6 octahedral linking. Linkage occurs through corners and edges (Figure 1.1). The density of the crystals is inversely proportional to the number of shared edges. This may be due to the increase in Ti-Ti interatomic distance which is 2.959 Å in rutile and 3.039 Å in anatase. Additionally, anatase has eight unit cells that make up one crystal as opposed to two unit cells for rutile.[2]

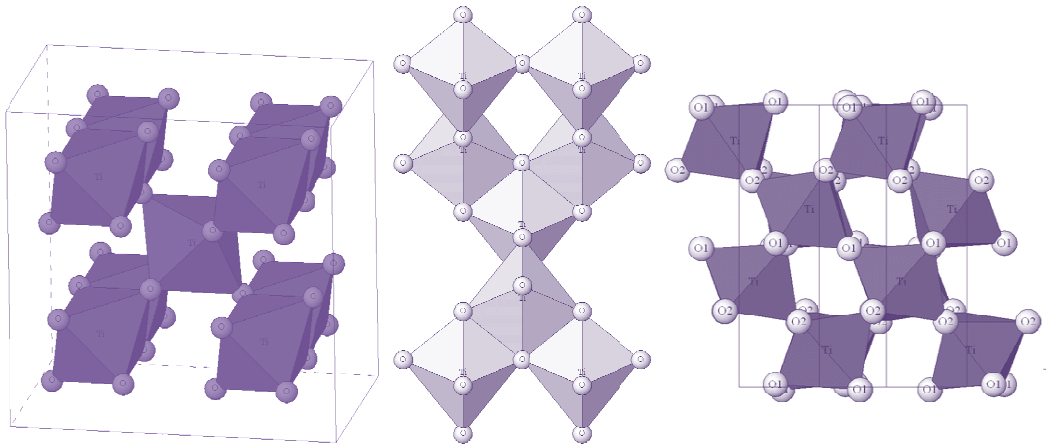

Figure 1.1. TiO_2 structural polymorphs (coordination number of Ti=6, two unit cells linked by various corners and edges)[3]

1.2 NANOSTRUCTURE SYNTHESIS

There are many processes used by the industry to manufacture nanomaterials and nanocomposites. The general mechanisms for TiO_2 are presented below: [4]

- gas phase processes (i.e. flame pyrolysis, high temp. evaporation and plasma synthesis);
- vapour deposition synthesis;
- liquid phase methods (i.e. colloids by chemical solvent reactions); and
- mechanical processes including grinding, milling and alloying.

The most common TiO_2 modification is through liquid phase methods (Figure 1.2). The monolith architecture can also be used for thin film and mesaporous film synthesis. However, nanoparticles are the most common form of titania for academic laboratory research and commercial applications as introduced earlier. They are also used in compound form for more advanced synthesis of nanostructures. Since nanostructures are the most relevant to the present research, titania nanoparticle review will end here.

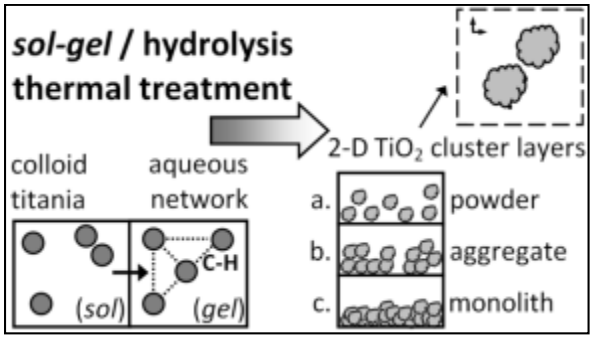

Figure 1.2. TiO_2 nanoparticle synthesis review

There are currently three main ways to modify TiO_2 beyond the first dimension. Varying from the lowest to highest effective surface areas, they are horizontal nanotube clusters, vertical nanotube arrays and nanowires. The corresponding synthesis techniques require stringent process control with pre- and post-processing.

TiO_2 nanotubes are somewhat straight and short sections of thin walled tubing. They are generally synthesized through hydrothermal techniques. Such techniques require a mixture of titania nanopowder with an aqueous solution of NaOH. The relative constituent amounts determine nanotube purity and size. Ions may also be introduced in this step for additional modification yet the study so far is undeveloped. The mixture is then hydrothermally treated at temperatures up to 300 ^{o}C for over 48 hours. To complete the process, the precipitate is filtered and then washed with deionized water and with alcohol before drying.

The basic formation mechanism is driven by H-deficiency which leads to layer sheet cleavage and the formation of sheet-rolled multiwalled spiral nanotubes.[5] Residual anatase nanoparticles are clearly evident at low treating temperature and short duration (Figure 1.3).[6] However, these nanotubes are under speculation concerning their formation and construction. Some researchers claim they do not share TiO_2 properties and cannot be considered a pure titania construction. The Ti/O atomic ratios vary and the anatase phase could not be repeated.[7]

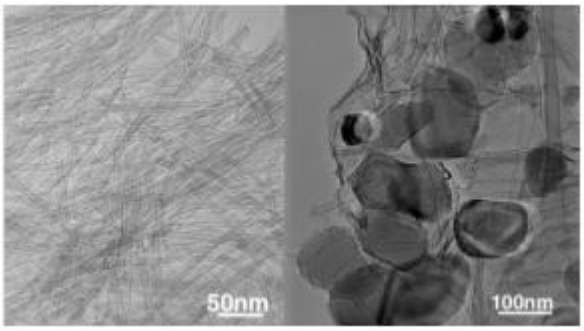

Figure 1.3. TEM scans of high-purity nanotubes at optimum conditions (left) and sub-optimum conditions (right)[6]

The vertical nanotube arrays are typically 50 nm in diameter with thin walls. They are synthesized on a level substrate either with a template (Figure 1.4) or by anodization bath chemistry. Titanium isopropoxide is oxidized in a reagent mixture at around 500 ^{o}C. Same as for the planar nanotubes described earlier, the process is completed by repeated washing steps.[8]

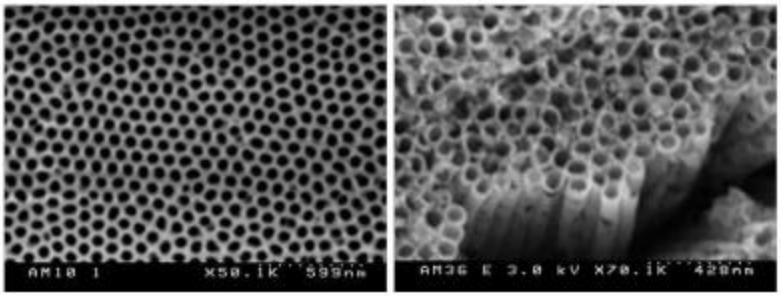

Figure 1.4. Porous anodic alumina (left) used as a template for titania nanotubes (right)[8]

Pre-process doping is also possible. For example, annealing titanium foils and titania films in a hydrocarbon flame forms carbon-doped titania. With the anodization process, doping may be performed during the chemical bath process. Here, N has proven to be an effective substitutional element due to its comparable ionic radius and p-state compatibility with oxygen. Additionally, anodization experiments offer a high resultant sensitivity to titania nanotube morphology by changing applied voltages, electrolyte concentration and oxidation times. [9]

In contrast to titania nanotubes, titania nanowires are amorphous with no hollow core. Nanowire diameters can range from 20 nm to 200 nm with lengths up to several centimeters. The resulting 2-D layering is also the closest architecture to a fully 3-D network (Figure 1.5). Nanowire synthesis is most developed with electrospinning. Electrospinning relies on a precursor anode accelerated by high voltage from the Taylor cone to the cathode target. The precursor is a mix of poly(vinyl pyrrolidone or acetate) and titanium tertaisopropoxide in an alcohol solution. A conversion to anatase requires calcinations at about 500 ^{o}C in air. The controllable parameters include precursor mixture concentrations, applied voltage and the precursor feeding rate.[10]

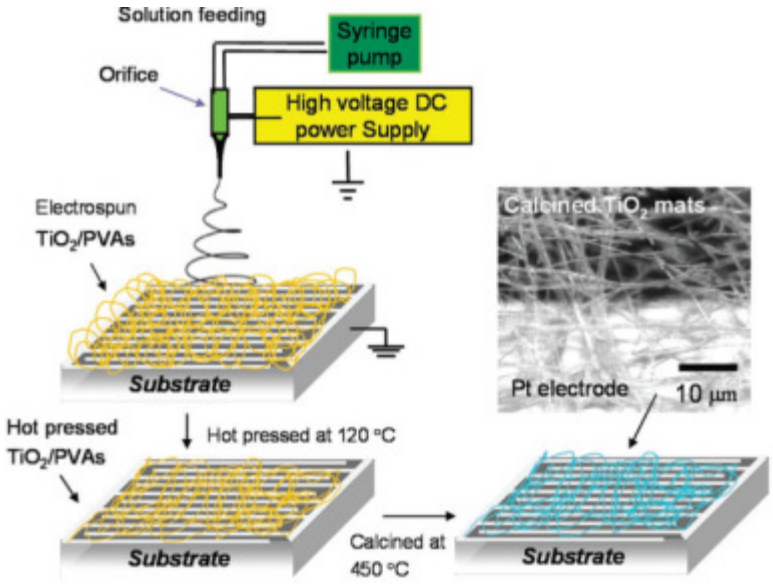

Figure 1.5. Electrospinning process of TiO_2, SEM scan inset[10]

1.3 PREVIOUS LAB GROUP STUDIES

In the lab that this research was performed, it was first predicted by Tan and Venkatakrishnan (2008) that it may be possible to form nanofiber structures from titanium by femtosecond laser ablation with MHz pulse frequency at ambient room conditions.[11] This theory was based on similar results from irradiating Group XIII and Group XIV materials including graphite, lead, aluminum, tin, glass and Sn-In-Pb-Bi compound. The study was continued by Sivakumar et al. (2010) and found that irradiation of Ti can lead to a formation of rutile phase structures and generalized that 2 MHz – 1msec results in the threshold laser fluence for nanostructure formation[12]. Tavangar et al. (2011) applied TiO_2 nanofibers in the biomaterials application using 4, 8, 12 MHz – 5 msec parameters. These parameters were thought to have varied surface porosity. Both rutile and anatase phases were found by X-ray diffraction analysis.[13]

However, these synthesis parameter studies were severely lacking optimization. There is no way to generalize how a molecular sensor may perform based on these preliminary experiments. For example, 26 MHz is thought to have much better repeatability [14] yet was not studied for

TiO_2 synthesis. Also, the network depth study is crucial in understanding the effects of confocal detection volume for Raman scattering. The irradiation times could have significant impact on detection capacity by a nanofibrous network, yet only the 5 msec dwell time was chosen in previous trials. This study will continue on the knowledge built up from previous work on TiO_2 3-D network nanofiber synthesis to develop a functioning molecular sensor for Raman spectroscopy.

1.4 MOLECULAR SENSING

Nanoparticles (NPs) provide a special interface for adsorbed molecules. As introduced to this research, Ag and especially Au nanoparticles possess highly active molecular properties. Firstly, NPs can immobilize molecules. Electrostatic interactions are common where some molecules can have preferential adsorption based on NP charge. Secondly, nanoparticles can act as a catalyst in electrochemical reactions. Thirdly, NPs can enhance electron transfer. [15] Although once again this makes Au and Ag very popular for sensing applications, TiO_2 is likewise dominant in dye sensitized electron injection such as for solar cell applications.[16] Consequently, such chemical adsorption affinity to TiO_2 has yet to be exploited for molecular sensors.

Current molecular detection assisted by TiO_2 is through electrochemical methods. In particular, cyclic voltammetry is the most popular detection method of biosensors. It relies on minute changes in registered current as a result of adsorbed biomolecular species through functionalized surfaces. The functionalization is performed by electrochemical immobilization of a particular enzyme receptor (eg. glucose oxidase). The electrochemical oxidation of hydrogen peroxide (H_2O_2) is typically used as a proof of biosensor performance.[17]

At the same time, cyclic voltammetry has profound drawbacks that require stringent process control for dependable and repeatable results. For instance, the oxidation of H_2O_2 requires high overpotential where noise from other oxidizable species is present. In this range TiO_2 is an insulator and cannot be used directly for electrochemical studies. Therefore, mesoporous TiO_2 films serve mainly for diffusion control purposes (Figure 1.6). TiO_2 films however do exhibit an electrocatalytic affinity towards H_2O_2 reduction in the presence of dioxygen.[17]

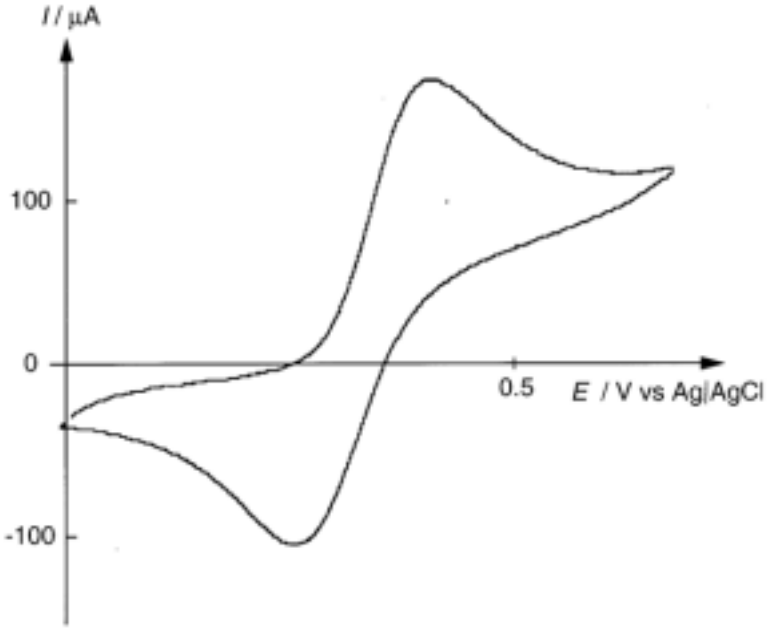

Figure 1.6. Cyclic voltammogram showing quasi-reversible redox signal of ferrocyanide on SnO_2 as diffused through the semi-conducting TiO_2 mesoporous film[17]

Gas sensing is another popular TiO_2 sensing application. Gas sensing is needed for industrial process control, combustion control and medical applications. At elevated temperatures (upwards 600 ^oC), TiO_2 is non-stoichiometric and its resistance changes upon gas exposure. This property has previously enabled successful detection of carbon monoxide[18] and NO_2.[10] Titania nanotubes with chemisorbed hydrogen have also shown changes in resistivity by removing chemisorbed oxygen (at ca. 300 ^oC). [19] To better explore the molecular sensing potential of

TiO_2 beyond gas at elevated temperature, more of the emphasis has to be on its optical properties.

In Raman spectroscopy, electromagnetic radiation (commonly visible laser light), is applied incident to a surface. Three phenomena may occur with six possible interactions (Figure 1.7). First of all, the light may transmit through the substrate and there will be no signal. Second, the light may be absorbed as energy by the surface (infrared, absorption and absorption-fluorescence). The third option is that light may scatter (Raleigh, Stokes and anti-Stokes). The amount of scattered light depends on the first two factors. To enhance the Raman signal, it is desirable to promote conduction band electron (i.e. plasma) coupling as much as possible.

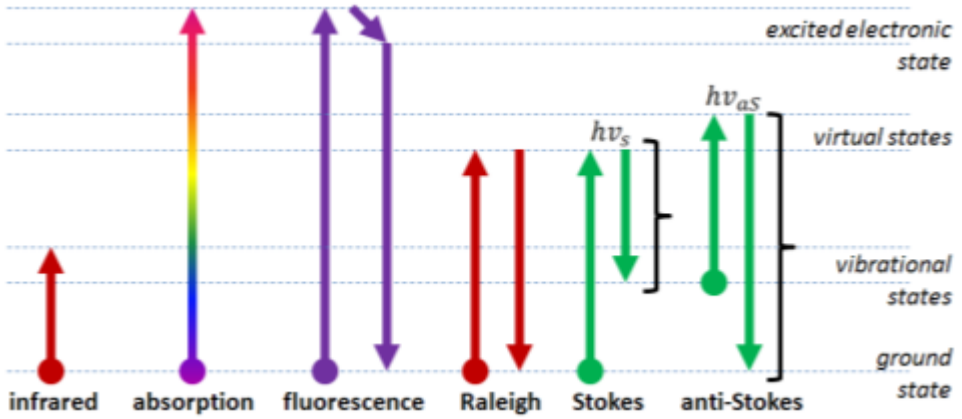

Figure 1.7. Light interaction with a surface where the relative colours represent typical wavelengths used in experimental setups

Surface-enhanced Raman spectroscopy (SERS) is the main focus of this study. The technique relies on special nanostructuring of materials to achieve localized surface plasmon resonance (LSPR) which enhances the Stokes-shifted EM fields. Au and Ag boast unperturbed plasmon resonance and hence simple nanoparticle geometry is enough to provide the highest SERS sensitivity to date. For other materials such as TiO_2, the high dielectric damping and poorly defined conduction band electrons demand advanced nanomanufacturing techniques to achieve

comparable SERS activity. A sub-category of SERS is resonance SERS (i.e. SERRS) where the excitation wavelength is matched to the maximum absorbance of the molecule being investigated. Another sub-category is tip-enhanced Raman spectroscopy (TERS) that relies on probe microscopy (such as atomic force i.e. AFM) to enhance the local EM field.

Coherent anti-Stokes Raman spectroscopy (CARS) uses two laser beams to generate a coherent anti-Stokes frequency beam, which can also be enhanced by resonance of a particular vibrational mode. The advantage is that the coherent nature of CARS can be more sensitive than spontaneous Raman microscopy. This in turn significantly reduces the average laser excitation power from mW to μW regimes. This is an important result as some chemical and biological systems have low EM damage thresholds. Sensitive aqueous epithelial cell mapping was demonstrated by Volkmer et al. (2000) by using this technique (Figure 1.8).[20]

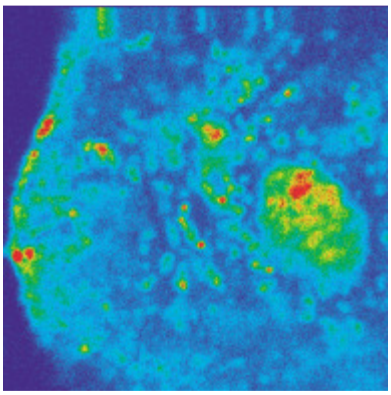

Figure 1.8. Epithelial cell DNA mapping using the 1000 cm^{-1} wavenumber for CARS[20]

Raman spectroscopy relies on a charge-coupled device (CCD). Since visible light excitation is used, the CCD is usually a visible light detector of scattered energy. For some samples, fluorescence may dominate the acquired spectra therefore demanding the use of longer infrared wavelengths. In this case, interferometers are used instead of CCDs. Fourier transform (FT) is

necessary to translate the acquired data to the frequency domain. However, FT infrared Raman methods are limited due to lower spatial resolution as dictated by wavelength dependency.[21]

Raman vibrational spectroscopy has evolved into a real-time analytical tool for species characterization. It is label free, non-invasive and unaffected by water in aqueous solutions.[22] As mentioned, SERS relies mainly on unperturbed plasmonic resonance. This makes various nanoparticle geometries of Au,[23] Ag [24] and Au-Ag composites [25] popular for optofluidic and chromatography SERS devices. However, Au typically needs a surfactant for stabilization such as toxic cetyltrimethylammonium bromide (CTAB).[26] As well, smaller Au nanoparticles tend to be used despite worse SERS performance. Ag is several orders of magnitude more SERS active than Au,[27] but the notorious oxide layer of Ag induces fluctuations in SERS as well as Raman laser-induced structural changes.[28]

On the other hand, TiO_2 is thermodynamically stable,[29] attracts water and water soluble molecules,[30] favorable for bio-molecular bonding [31] and it is corrosion resistant with a stable oxide surface.[26] The 3-D nanofibrous network presented here features additional characteristics in favor of species detection by SERS. Firstly, the high dielectric damping of TiO_2 is alleviated by various electromagnetic phenomenon of the nanofiber such as the nanogap, nanocluster and plasmonic hybridization. Secondly, the depth of the nanonetwork fully utilizes the laser's confocal volume for detection of Stokes shifted photons. Thirdly, the porosity controls molecular diffusion which is critical in micro-spot sized optical spectroscopy techniques.[32] In this study, controllable surface roughness and porosity which was directly related to SERS activity of BPA and DSS was investigated. These findings directly impact SERS sensor pad development towards chemical and bio-molecular sensing applications.

1.5 RESEARCH OBJECTIVE

The objective of this research is to use traditionally inactive TiO_2 for Raman sensing applications to be directly competitive to commercial Ag and Au Raman sensors. There are three main tasks to complete towards this objective:

1. Characterize which nanofiber network features are tunable towards Raman sensor development:
    a. synthesis parameter effects;
    b. morphology;
    c. phase constituency; and
    d. mechanical properties.
2. Evaluate the TiO_2 Raman performance activity:
    a. contributing EM mechanisms;
    b. test the sensor SERS response from different nanofibrous networks (variable by synthesis parameters); and
    c. determine the Raman enhancement factor.
3. Demonstrate molecular sensing capacity:
    a. crystal violet;
    b. bisphenol-A;
    c. diclofenac sodium; and
    d. develop sensor engineering criteria.

CHAPTER 2

RAMAN SPECTROSCOPY OF TITANIUM DIOXIDE

The crystal structure of TiO_2 phases was first studied in 1916 by Vegard with model refinements as late as 1970s. The peak positions are characteristic of lattice vibrations. This means that although the peak intensity may vary, the Stokes shifted peak wavenumbers (cm^{-1}) cannot shift significantly without crystallographic modification. Nonetheless, optical phenomenon such as peak splitting may occur and give rise to additional peaks.

2.1 PLASMONICS

The collective conduction electron resonance of an ion metal core is referred to as plasmonics. Plasmonic studies are necessary in explaining TiO_2 nanoparticle EM activity. The resonance frequency for bulk plasma is represented by Eq. 2.1. [33]

$$\omega_p^2 = \frac{ne^2}{\varepsilon_o m} \qquad \text{Eq. 2.1}$$

where *n* is the number density of mobile charge carriers, *e* is the carrier charge, *m* is the carrier mass and ε_o is the relative permittivity of free space. EM radiation, such as visible laser light can be used to excite this plasmonic resonance. If ω_p is above the incident frequency, the charge carriers will reflect the incident waves. For example, ω_p for TiO_2 is in vacuum UV which means visible light will be reflected and TiO_2 will appear white—as it does. Localized Surface Plasmon Resonance (LSPR) occurs when ω_p equals the incident frequency. It is common to describe the vibrational frequencies in terms of wavenumbers (cm^{-1}) which are obtained by dividing the actual frequency by the velocity of light or by inverting the wavelength.[34]

The highest degree of phonon confinement is three-dimensional, where quantum dots and NPs internally reflect the energy by the surface interface. A tuneable confinement response (i.e.

changes in the dielectric properties) results in various Au and Ag NP visible colors as applied in antiquity with paintings and glass decorations.[34] This phenomenon is also applicable to molecular sensing as the absorption wavelength (extinction maximum spectra) can vary by applied analytes.[35]

2.2 CHARACTERISING SPECTROSCOPIC PEAKS

To determine the Raman frequencies analytically, it is necessary to determine the force constants of the crystal lattice. One way to approach this problem is by potential energies and force constant empirical assumptions. The difficulty with empirical results is that the peaks may slightly deviate due to stoichiometric deviation of TiO_2 varying by preparation techniques.[36]

Crystals with discrete molecules or ions may exhibit vibrations of the lattice structures.[37] For TiO_2 there are two molecules with six atoms per cell which corresponds to 15 possible vibration modes.[38] Vibrational modes have been developed and represented in non-reducible forms. From such, it was found that some vibration modes are Raman active. Other modes are active in infrared parts of the electromagnetic spectrum or not active at all.

Based on the vibrational response, the incident energy may be Stokes (energy loss) or anti-Stokes (energy gain) shifted or Raleigh scattered. However, only the Stokes shift is usually detected in Raman spectroscopy. For Raman activity, the molecular polarizability must change. For infrared activity, the dipole moment must change. This is demonstrated by Figure 2.1.

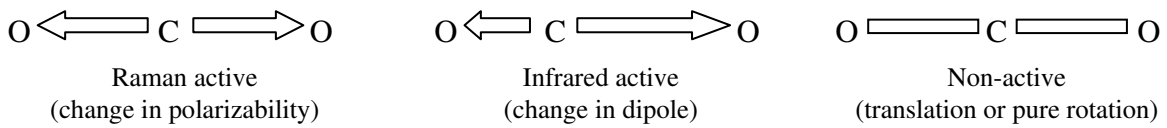

Figure 2.1. Variations in energy shifts determining activity for CO_2 [37]

In addition to fundamental modes of vibration, secondary peaks may be realized whenever there is more than one atom in a molecule. As a result, there is greater uncertainty in obtained results if, for instance, there are too many peaks close together making it difficult to differentiate between states (such as with two phonon scattering). However, the total scattered intensity would increase.

2.3 RUTILE PHASE

In total, rutile has 15 optical modes.[39] Figure 2.2 shows that the E_u mode has three combinations that are doubly degenerate, or two couples that tend to reduce the lattice momentum. The B_{1g} mode however tends to enhance the lattice momentum therefore it is a generate type.

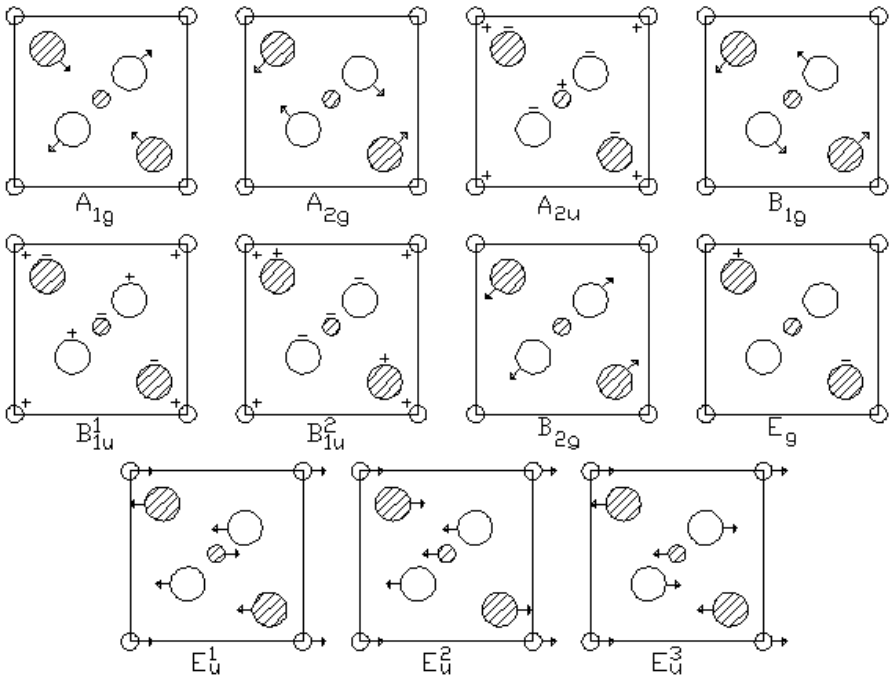

Figure 2.2. Lattice vibrations of rutile, small circles represent Ti atoms, the large circles represent O atoms and shaded indicates out of plane, the basal plane is represented, where `+` indicates above and `-` indicates below the basal plane [39]

The character table of the point group D_{4h} shows irreducible representation for the 15 optical modes given by Eq. 2.2:[37]

$$1A_{1g} + 1A_{2g} + 2A_{2u} + 1B_{1g} + 1B_{2g} + 2B_{2u} + 1E_g + 4E_u \qquad \text{Eq. 2.2}$$

However, from Eq. 2.2, one A_{2u} and one E_u mode are translations—and as with pure rotations—are not considered for spectroscopy. The vibration modes representation for rutile are reduced from Eq. 2.2 and shown below by Eq. 2.3:

$$\left(1A_{1g} + 1B_{1g} + 1B_{2g} + 1E_g\right)_{Raman} + (1A_{2u} + 3E_u)_{infrared} + \left(1A_{2g} + 2B_{2u}\right)_{inactive} \qquad \text{Eq. 2.3}$$

The result from Eq. 2.3 is to expect four Raman active frequencies and four infrared active frequencies. The Raman active frequencies have been analytically determined by Dayal by determining force constants through potential energy and empirical assumptions with results presented here for the Raman active frequencies by Eq. 2.4:[39]

$$\begin{aligned} A_{1g}&: 4\pi^2\upsilon^2 m = 1.8K_1 + 2K_2 + .32K_3 \\ B_{2g}&: 4\pi^2\upsilon^2 m = 1.8K_1 + 2K_2 + 5.3K_3 \\ B_{1g}&: 4\pi^2\upsilon^2 m = .32K_3 \\ E_g\ &: 4\pi^2\upsilon^2 m = .6K_1 + 2.34K_2 + 2K_3 \end{aligned} \qquad \text{Eq. 2.4}$$

It may be noticed from the above equation set that the mass of Ti atoms or M does not affect Raman active frequencies. This is because the Ti atoms are at rest in Raman active modes and only O atoms with mass m are resonated at frequencies υ. Moreover, mode B_{1g} is degenerate where all atoms resonate in phase.[39] However, B_{2g} is also degenerate and has the largest multiplicative factors. Consequently, B_{2g} is expected to have the highest resonant frequency. On the contrary, Ti atoms will oscillate in infrared modes. A summary of experimental data for Stokes shifted energy for rutile is shown by Table 2.1.

Table 2.1. Observed spectrum and associated vibrational modes of rutile

	Intense Bands (cm^{-1})	Vibration mode	Broad Bands (cm^{-1})	Vibration Mode
Raman	609 [40] 611 [37] 612 [38] [41] [42]	A_{1g}	143 [38] [42] 144 [37] [41] 154 [40]	B_{1g}
	446 [40] 447 [38] [42] 448 [37] [41]	E_g	826 [38] [42] 827 [41] 828 [37]	B_{2g}
Infrared			183 388 500 [38] [42] 515 [43]	E_u (TO)
			373 458 806 [38] [42] 352 423 608 [44]	E_u (LO)
			167 [38] [42]	A_{2u} (TO)
			811 [38] [42] 695 [44]	A_{2u} (LO)

The Raman active peaks are demonstrated by Figure 2.3 for rutile.[40] The 239 cm^{-1} peak is a combination peak that is related to the B_{2g} mode. This phenomenon is observed by varying the preparation technique. Variations in vibration mode wavenumbers could be expected as summarized earlier by Table 2.1.

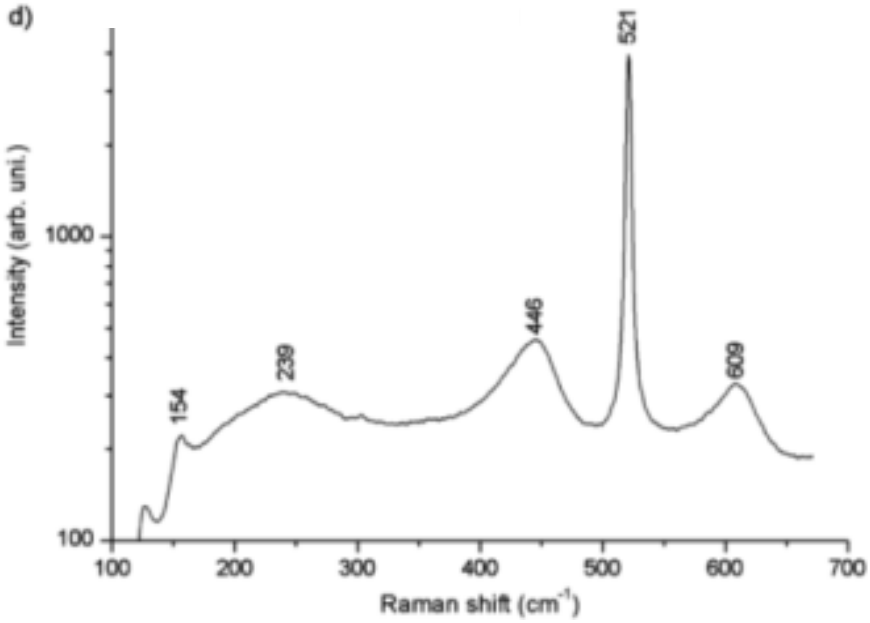

Figure 2.3. Raman spectroscopy of rutile, the 521 cm^{-1} peak results from the Si substrate[40]

2.4 ANATASE PHASE

Two-phonon scattering is weaker in anatase than in rutile. Moreover, rutile exhibits stronger scattering under second-order vibrations. Therefore, it is expected that anatase will have sharper intensities than rutile.[44] The lattice vibration representations are shown by Figure 2.4.

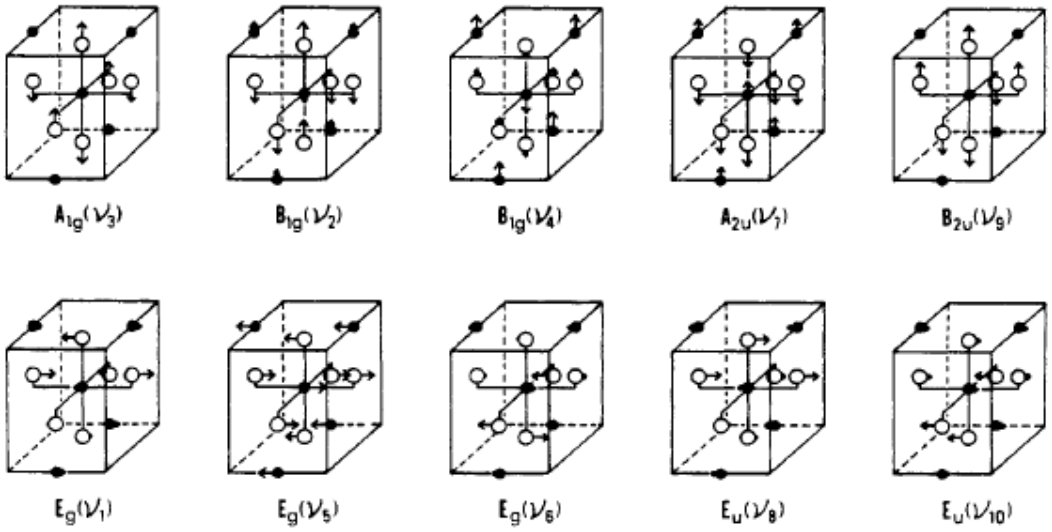

Figure 2.4. Lattice vibrations of anatase, solid circles are Ti, hollow circles are O atoms, the basal plane is midway up the represented cubic[1]

The character table of the point group D_{4h} shows irreducible representation for the 15 optical modes and is given by Eq. 2.5: [1]

$$\left(1A_{1g} + 2B_{1g} + 3E_g\right)_{Raman} + (1A_{2u} + 2E_u)_{infrared} + (1B_{2u})_{inactive} \qquad \text{Eq. 2.5}$$

The result from Eq. 2.5 is to expect six Raman active frequencies and three infrared active frequencies. A summary of experimental data for Stokes shifted energy for anatase is shown by Table 2.2.

Table 2.2. Observed spectrum and associated vibrational modes of anatase

	Intense Bands (cm^{-1})	Vibration mode	Broad Bands (cm^{-1})	Vibration Mode
Raman	398 515 [41] 400 515 [37] 397 [40] 408 [36] 410 [36]	B_{1g}	624 [36] 630 [36] 639 [40] 640 [37] [41]	E_g
	515 [41] 519 [37] 520 [36]	A_{1g}		
	144 197 [37] 145 197 [40] 147 198 [41]	E_g		
Infrared			525 [44]	A_{2u} (TO)
			347 700 [44]	E_u (TO)

The Raman active peaks are demonstrated by Figure 2.5 for anatase. Notice that it is difficult to resolve the second resonance of the B_{1g} and the fundamental A_{1g} modes at 521 cm^{-1}. Variations in vibration mode wavenumbers could be expected as summarized earlier by Table 2.1.

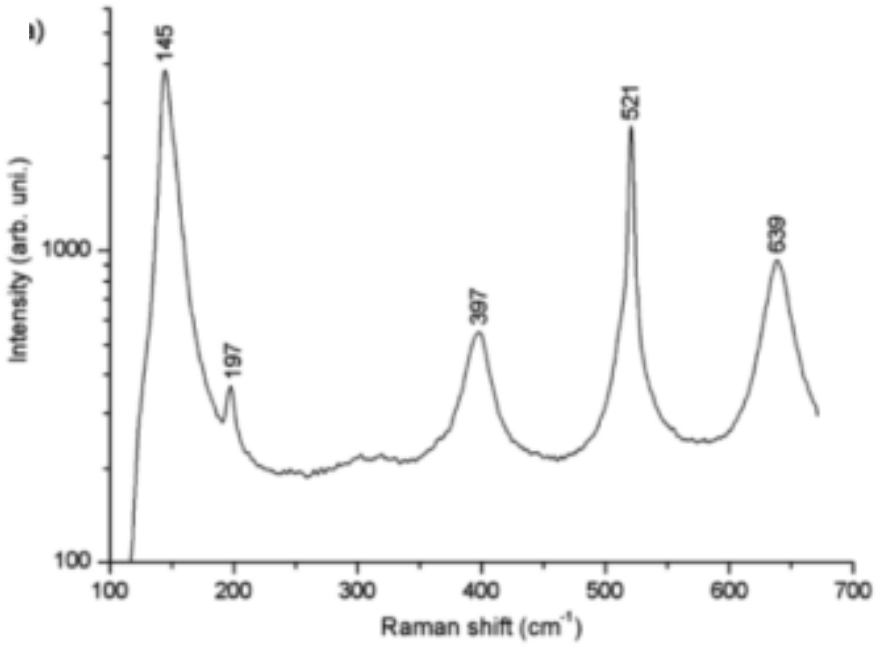

Figure 2.5. Raman spectroscopy of anatase, the 521 cm^{-1} peak results from the Si substrate[40]

CHAPTER 3

EXPERIMENTAL MATERIALS AND METHODS

There were three major experiments carried out under this study. The first experiment used Raman spectroscopy to track the surface enhancement between varying laser patterning parameters. The second set dealt with crystal violet (CV) dye enhancement. The third set of experiments dealt with the application of two aromatic chemicals with varying laser patterning parameters. The equipment used and materials are summarized in this section.

3.1 FEMTOSECOND PULSED LASER

A pulsed Yb-doped fiber amplified femtosecond laser was used to generate TiO_2 nanofibers from a commercially pure Ti substrate. To reduce the already large number of synthesis combinations, the laser central wavelength (515 nm as a generated second harmonic), power (16 W), pulse duration (214 fs), polarization (circular) and piezo scanning speed (1000 µm/sec) were kept constant under single mode-locked pulse irradiation. These parameters were selected based on the earlier investigation of Ti nano-fiber synthesis.[12]

Variations in pulse repetition (2, 4, 8, 13 and 26 MHz) and the effective number of pulses (1, 5, 10, 15, 20 and 25 msec duration) were carried out to see the effect on nanostructure generation and characteristics. The 5x5 mm area with 50 µm point spacing irradiation array pattern was first plotted on EzCAD© software. Once galvanometer scanning was initiated, the acousto-optical modulator blocked irradiation between successive points. As a result, the intensity of the laser beam becomes time averaged and may vary from zero to more than 85% of the incident beam [45]. The general setup is represented by Figure 3.1. It is also readily possible to design various channels and junctions if desired.[46]

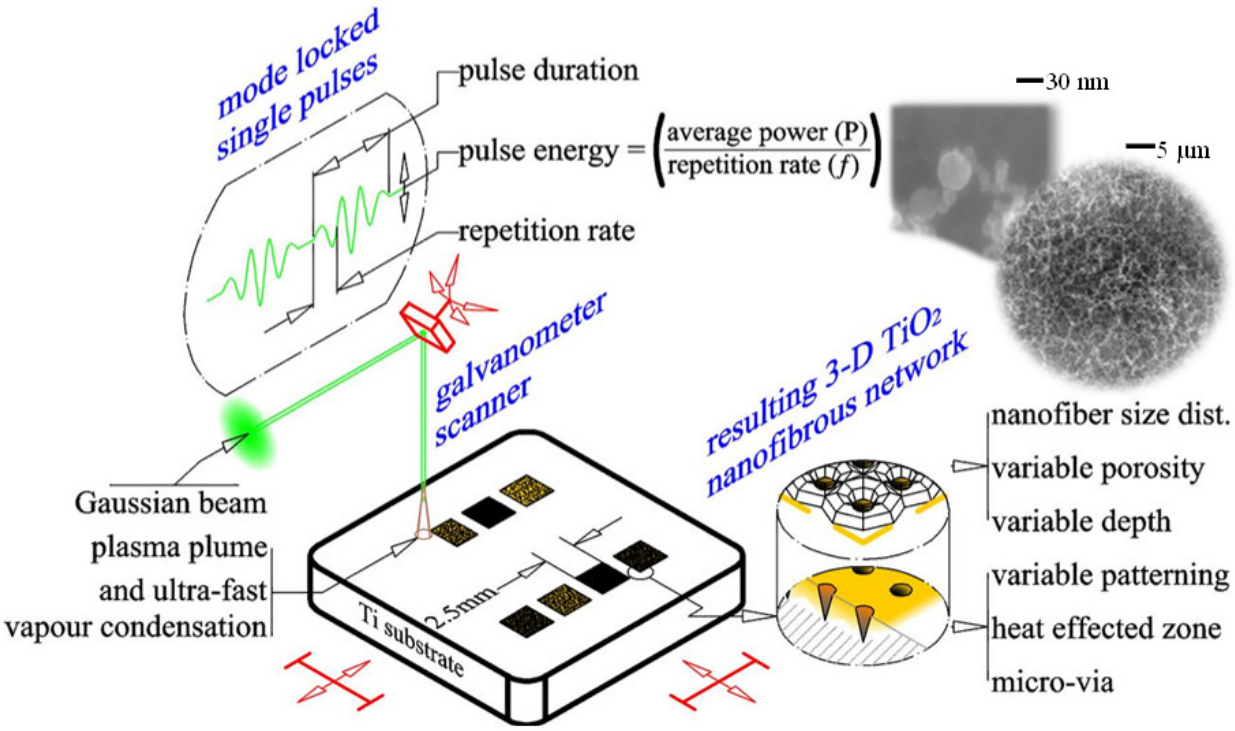

Figure 3.1. TiO_2 nanofibrous network sensor pad synthesis tailored towards favorable SERS interface characteristics

The average fluence per target area is defined as the average power per laser spot area or alternatively represented as:

$$\phi_o = 4P / \pi f \omega_o^2 \qquad \text{Eq. 3.1}$$

where P is the average femtosecond laser power (16 W), ω_o is the theoretical spot size diameter (m) and f is the laser repetition rate. Transverse irradiance patterns (TEM modes) may be manipulated for varying spot image projection. By suppressing the gain near the edges of the beam, a fundamental TEM_{00} mode is achieved. This mode focuses a single spot with a Gaussian transverse profile and a nearly spherical wavefront. The theoretical laser spot is therefore: [47]

$$\omega_o = 2\lambda F / \pi \omega_b \qquad \text{Eq. 3.2}$$

where λ is the laser wavelength (515 nm), F is the effective telecentric lens focal length (12.478 mm) and ω_b is the beam waist diameter (8 mm).

The minimum irradiation fluence required may be achieved by a single pulse or multiple pulses in a short timeframe.[46] From Eq. 3.1, it may be seen that with an increasingly smaller machining spot radius, it is necessary to increase the power for the same fluence. Yb-doped fiber amplification was critical in this research to achieve the sub-micron spot radii. Yb-doping is ideal for fsec pulse amplification while retaining a high degree of efficiency.[48]

Irradiation laser fluence was considered to investigate the TiO_2 network synthesis parameters. Multiple pulses are more efficient than single pulses due to a threshold reduction. The threshold fluence reduction by the incubation principle after Jee et al. (1988) is represented as: [49]

$$\phi_{th}(n) = \phi_{th}(1)(tf)^{S-1} \qquad \text{Eq. 3.3}$$

where *t* is the irradiation dwell time (sec), f is the laser repetition rate (Hz), $\phi_{th}(1)$ is the threshold ablation fluence with one pulse (0.28 ± 0.02 J / cm^2 for Ti) and S is the incubation coefficient (0.83 ± 0.03 for Ti).[50] Appendix A.5 summarizes these effects for the parameter set of investigated sensor pads.

3.2 MATERIALS

Grade 2 commercially pure titanium (98.9%) was used in all experiments (0.125 in thick). The surface was finished by fine 600 grit sandpaper grinding. The surface was then carefully wiped clean with no applied chemicals.

Crystal violet (CV) is a popular dye used in SERS due to its large Raman cross-section. To test the TiO_2 substrate response, one drop of CV $8x10^{-3}$M (note: the "8" was previously not presented) solution was applied over the nanofibrous network through an 18g syringe needle. This procedure was repeated for the most active substrates determined earlier. The concentration

was chosen such that a clear Raman spectrum just begins to appear when using commercial Ti as the substrate.

To simulate pollutant detection using Raman signals under environmental conditions, drinking water was used as a solvent for BPA and DSS. No reporter molecules were used. Drinking water analysis revealed that Na, Ca, Cl and Cl^- are the most concentrated inorganic materials. SERS contributing elements were also studied but were found to be relatively negligible (Appendix A.1).

Dried residue and aqueous solutions of DSS and BPA were investigated under Raman spectroscopy. The aqueous solutions were mixed 1% chemical by volume with drinking water and applied immediately prior to Raman spectroscopy measurements. Dried residues were prepared the same way as the aqueous solutions, but subsequently dried on a hotplate at 60 ^oC. Both BPA and DSS are thermally stable at 60 ^oC.[51] Each particular experimental condition was repeated on average 5-7 times across different points for a particular sensor pad.

3.3 SURFACE CHARACTERIZATION

For surfaces with a high density of nanofibers, it was necessary to gold coat the nanonetwork due to excessive Scanning Electron Microscope (SEM) charging. Also, Energy Dispersive X-ray (EDX) analysis was carried out on a 1000x magnified area. The area was chosen such that several irradiated points were under the same analysis.

For transmission electron microscopy (TEM), a carbon grid was used to swab the sample and then the grid was scanned. During scanning, contamination was observed by a growing layer on the particles. This effect was minimized by varying TEM parameters as well as the physical setup. EDX analysis was also carried out across a single particle to verify the nanostructure

composition. This equipment was used at the Centre of Nanostructure Imaging, University of Toronto.

Low scanning speed AFM contact mode was used to penetrate the nanofibers and reveal the surface morphology. SEM was used to qualify the 3-D network porosity changes and general sensor pad topography. Scanning near-field microscopy (SNOM) at 514 nm with an aluminum coated fiber probe (nominal aperture 100 nm) was used to study optical roughness of individual micro-vias. Additional experimental details are presented with Appendix A.2.

Raman spectroscopy is particularly useful due to low spectral interference from water.[52] The Raman machine used a laser with a 532 nm wavelength at 100 mW. The irradiation power was reduced to 1 mW by using a D2 filter. The equipment limited lower wavenumber was 150 cm^{-1}. DSS and BPA spectra beyond 1650 cm^{-1} are lower intensity summation bands representing a minority of characteristic vibrational modes thence were not considered for acquisition.[53] The scattering energy parameters were chosen based on trial-and-error for repeatable spectra results with minimum noise. The exposure time was 7 sec with a five time repetition. A D2 filter (reducing power to 1 mW) with a 50x objective was used. No laser heating effect is expected under such conditions.[54] This equipment was used at the Institute of Optical Sciences, University of Toronto.

CHAPTER 4

NANOFIBROUS 3-D NETWORK

Nanofibers are quasi-organized nanoparticle clusters possessing special properties. For example, Song et al. (2009) demonstrated a sevenfold immunoassay improvement by using planar Au nanofibers.[55] Nanofiber inherent porosity also serves to control molecular diffusion that improves the Raman laser optical trap effectiveness.[24] For detection by SERS, traditional nanoparticle substrates are tunable mainly by the nanogap and nanocluster phenomenon.[23]

Figure 4.1 demonstrates the ability to control the nanofiber network and the surface support characteristics during synthesis. Increasing the effective number of laser pulses (msec) increases the nanofiber density. Lowering the pulse repetition (MHz) increases the laser fluence which in turn affects substrate morphology. The morphology resulting below 13 MHz (e.g. 8 MHz) is similar but with larger mean nanofiber particle sizes.

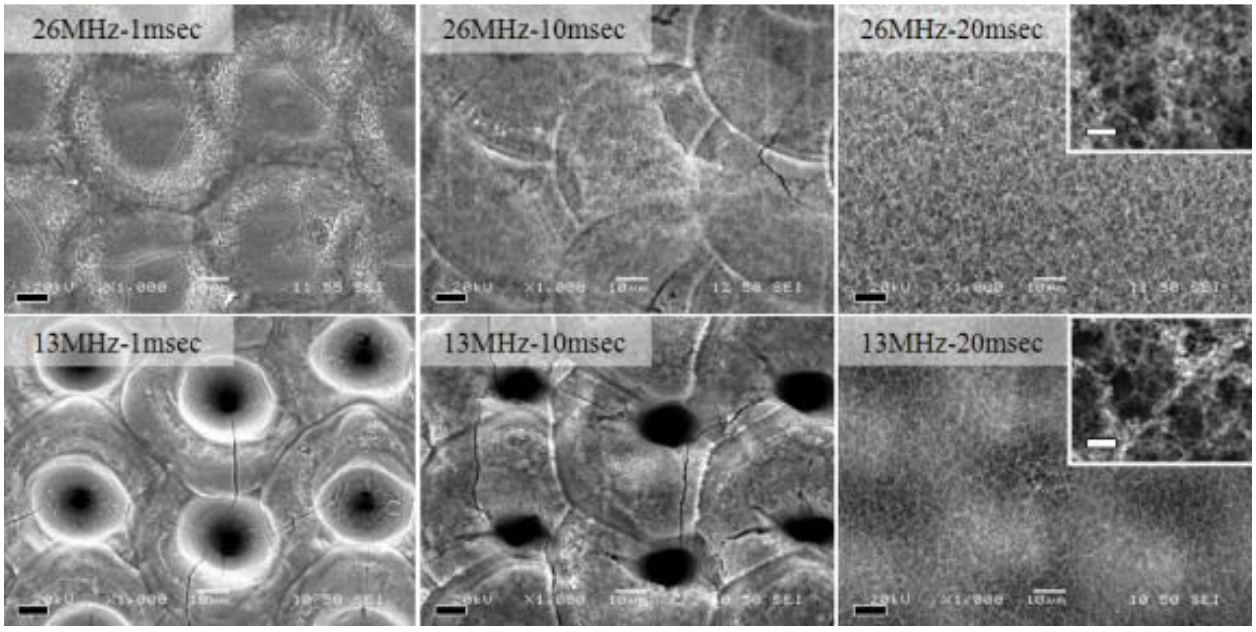

Figure 4.1. Summary of nanofiber generation and coverage for 26 MHz and 13 MHz laser pulse repetition rates and varying durations (SEM, bar scale is 10 µm-black and 1 µm-white)

It was found that morphological variations of the circular microvias (Figure 4.1) do not have a significant impact on the Raman detection of CV (Appendix A.2). This was an expected result since the nanofibrous network act as a porous support for CV adsorption and hence keeps the molecules in focus. The implication of this result is that the irradiation pattern of Figure 4.1 can be readily designed to include various channels and junctions.[46]

4.1 PLUME CHARACTERISTICS

When the laser is tightly focused on a target surface, a plume may form at the target depending on the material and the minimum laser fluence. The plume will then promote nanostructure nucleation. Whether these structures form when suspended in the plume or on the substrate under the plume pressure is so far under speculation.

One popular mechanism for explaining nanofeature formation is vapour condensation. In this technique, a vapour with a high pressure and temperature will initiate a plume.[12] It was noted that “smaller particles are attributable to nucleation and condensation of vapour in the plasma plume while larger ones are due to the explosion of molten material because of high plasma pressure”.[12] Such classical nucleation theories were originally developed for aerosol studies. They cannot predict nucleation rates of metals such as Ti with simultaneous oxidation to TiO_2 that occurs in the ultra-fast sub-ms regime. Such theories provide only a philosophical understanding and need further development towards femtosecond laser ablation simulations.

Zeng et al. have classified the plasma plume to consist of three propagation fronts (Figure 4.2).[56] The first one contains vaporized atoms and ions which move the fastest. The second front consists of clusters which make up the majority of emitted species. The last front is liquid droplets in the micron or submicron range.

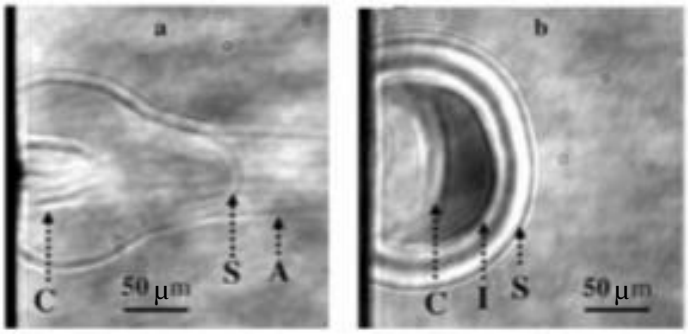

Figure 4.2. Plasma evolution for fs (left) vs. ns (right) lasers, notation as follows: S-shock front, I-ionization front, C-air breakdown plasma [56]

Femtosecond lasers have superior material processing features over longer pulse duration lasers. This is due to a high attainable resolution. Additionally, much lower laser fluence is required due to the absence of thermal losses.[57] This is also because for a femtosecond laser, the pulse is short enough that no significant plasma interaction occurs (Figure 4.2).

4.2 NANOFIBERS

Various TiO_2 nanomorphologies have been synthesized by other research groups including colloidal thin films,[58] nanotubes,[59] and nanorods[60]. However, the TiO_2 nanofibrous 3-D network is highly unique to this research group. The TiO_2 3-D network is composed of 15 – 150 nm diameter crystalline nanoparticles that are chained to form nanofibers (Figure 4.3). The nanofiber particle size distribution promotes good solute adsorption to larger nanoparticles while SERS stabilization is achieved by the smaller nanoparticles.[61] Micro-via effects on Raman spectroscopy have been included with Appendix A.2.

For TEM imaging, artificial structuring problems may arise when transferring the nanofibers from the substrate to the grid. As shown by Figure 4.3, the general morphology tends to remain the same. Nonetheless, when analyzing subsequent grid images, some distinction will be made

between nanoparticle aggregation resulting from the femtosecond pulsed laser synthesis and clustering due to grid transfer.

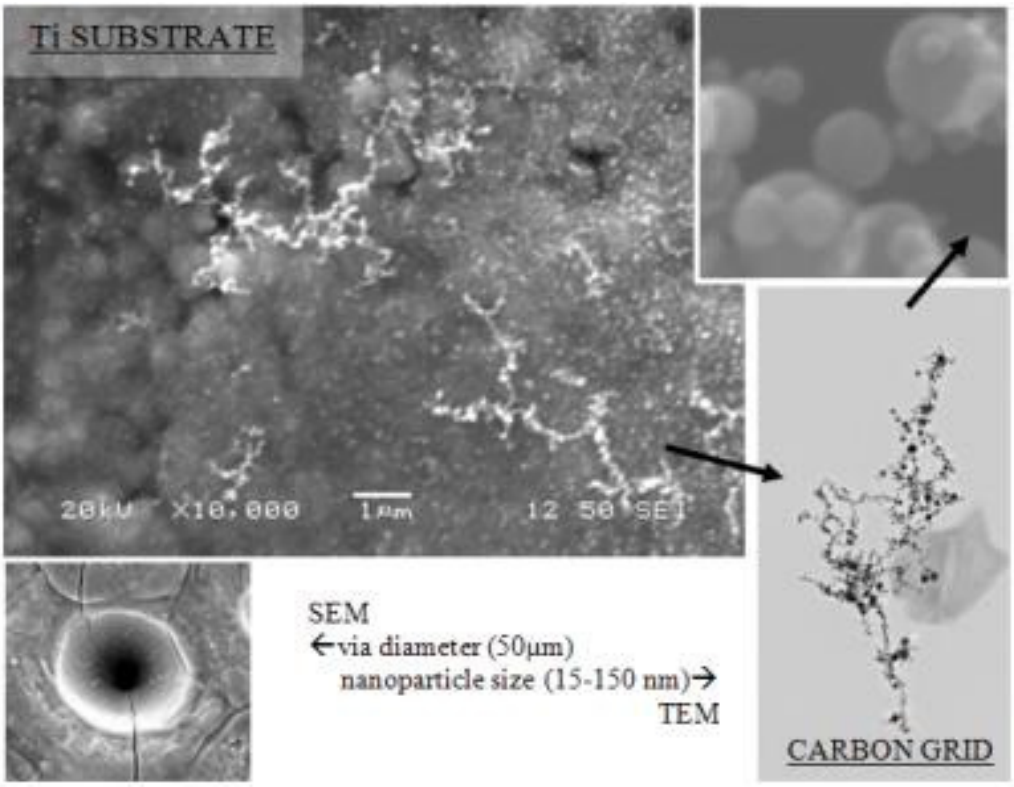

Figure 4.3. Initiation of TiO_2 nano-fiber formation; left side scans are SEM, right side is TEM

As the synthesis continues (msec regime), the fibers develop more intersection junctions (bottom right Figure 4.4). The junctions promote 3-D spatial growth within the plume and result in effective network stability and porosity. The top right inset of Figure 4.4 shows the developed TiO_2 nanofibrous 3-D network.

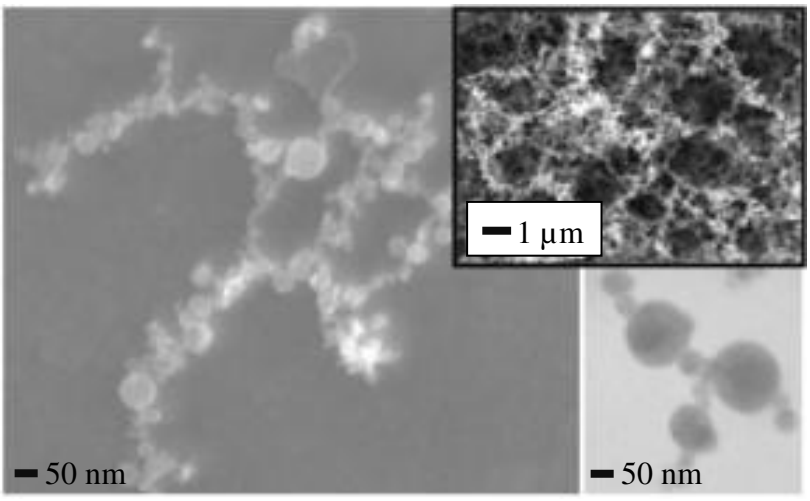

Figure 4.4. TiO_2 nanofibrous porosity development; images are TEM, top right is SEM

From Figure 4.5, O and Ti were identified by EDX and atomic weight was additionally determined to be 75% O and 25% Ti. Significant O content was expected due to the high irradiation temperature and instant oxidation of Ti.[11] Figure 4.5 also shows that O and Ti are in one crystalline state within the nanoparticle. This was indicated early on under TEM beam focusing by white diffraction spot convergence.

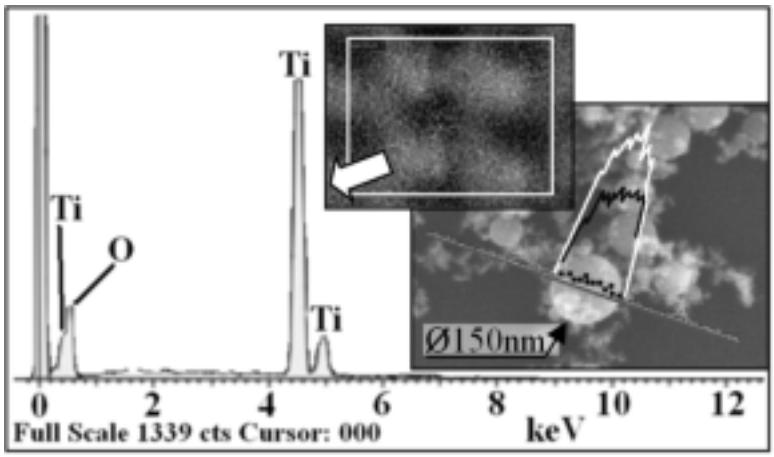

Figure 4.5. EDX analysis of TiO_2 nanofibers. The area scan window size is 100x80 µm. The white line section of the nanoparticle is Ti, the black line is O and the dotted line is phosphorous (background noise)

During the synthesis process, the nanofibers were collected from the plasma plume species on an Si substrate. The results are shown by Figure 4.6. The relative rutile to anatase phases change, in particular starting from predominantly rutile to predominantly anatase (see Raman Spectroscopy of Titanium Dioxide for details). When the nanofiber density is high enough, the anatase phase appears. It is reasonable to assume that the Raman signal is either enhanced for anatase and/or that anatase is the predominant phase constitution of the nanofibers.

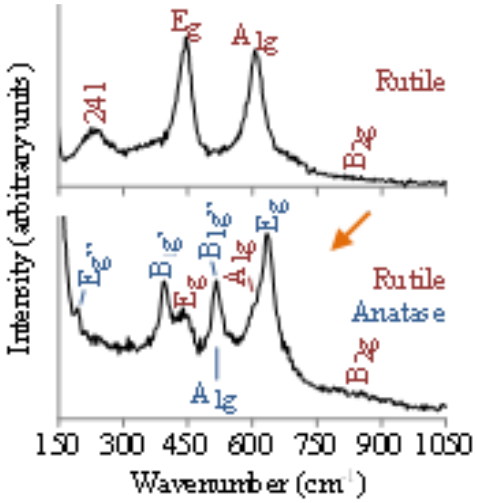

Figure 4.6. Raman spectra demonstrating synthesis parameter-variable TiO_2 phase compositions

In addition, the Raman spectrum inset of Figure 4.6 shows that it is possible to have a dominantly rutile or a mixture of rutile and anatase TiO_2 phases. Anatase forms at higher laser dwell time but more predominantly with higher pulse energy (especially below 13 MHz). TiO_2 conforms to D_{4h} symmetry with rutile modes detected as B_{1g} (144), E_g (443), A_{1g} (611) and B_{2g} (825) cm^{-1}. Anatase modes appear as E_g' (144), E_g'' (197), B_{1g}' (400), B_{1g}'' (515), A_{1g} (519) and E_g (640) cm^{-1}. TiO_2 peak shifting was minimal between the studied sensor pads and was likely affected by relative TiO_2 phase mixtures.

The mechanical properties of the TiO_2 nanofibrous network were also partially investigated. It was found the AFM contact probe imposes enough pushing force so as to glide through the nanofibers. This effect is shown by Figure 4.7. Whether there were nanofiber networks or not, the AFM scans revealed very similar images which are actually revealing the substrate morphology. This is an important result as it shows that the synthesized nanofibrous network may or may not have enough mechanical durability to maintain structural integrity with applied analytes for sensing. Moreover, the nanofibers may be loose enough as to float off the substrate and be freely suspended in the analyte solution. These issues will be investigated in Chapter 6.

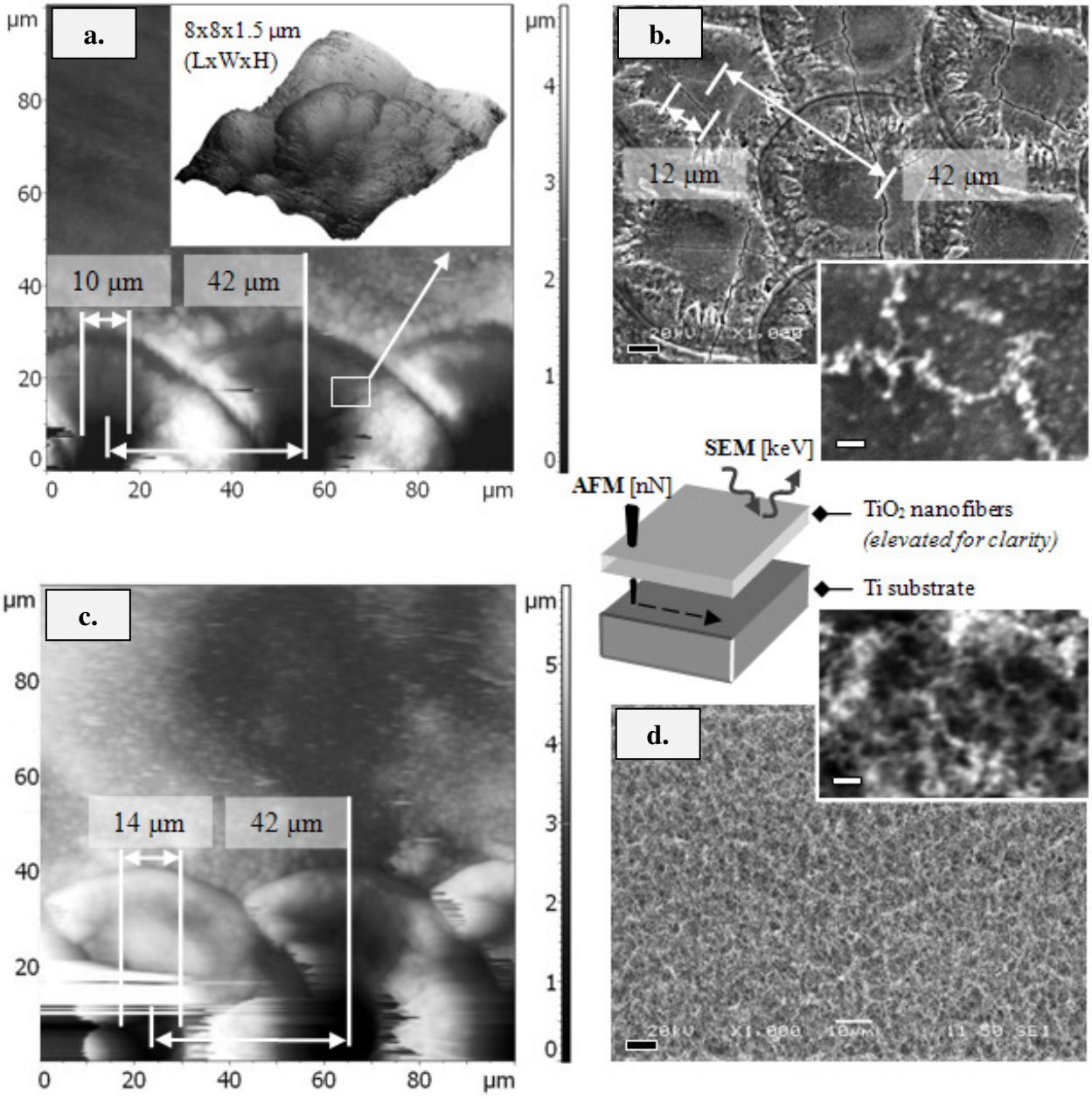

Figure 4.7. AFM (left side) and corresponding SEM (right side) for low density (top row) and high density (bottom row) nanofibers (SEM, bar scale is 10 µm-black and 1 µm-white). AFM black craters exceed the limiting 5 µm scanning depth

4.3 SUBSTRATE EFFECTS

The high temperature and pressure gradients induce rapid melting under non-equilibrium conditions.[62] In traditional nanosecond lasers, the generated heat is transferred to the substrate and may affect bulk properties. For femtosecond lasers, the time in which heat is dissipated into the material is slightly longer than the exposure time of the pulse. As a result, there is not enough time for the ablated area to be significantly heat affected. However, the sample in bulk may still substantially heat up due to plasma pressure and the specific conductivity of the bulk material. Figure 4.8 shows resultant cracking and plate sliding on the Ti surface. In particular, AFM scans reveal significant shear stresses built up as surface deformation is clearly evident.

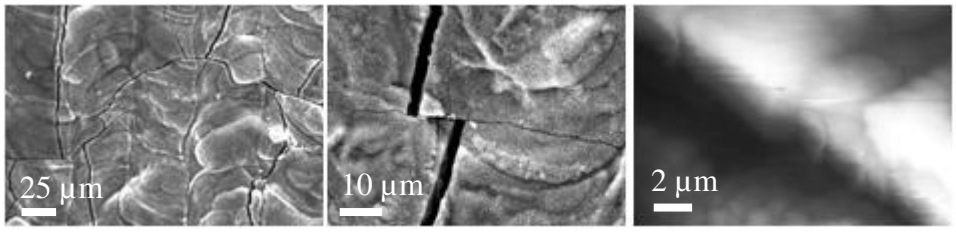

Figure 4.8. Thermal effects on the Ti substrate from femtosecond laser irradiation (left and middle are SEM scans, right scan is AFM)

Micro-via formation is a product of single point laser irradiation (Figure 4.9). The depth saturates with prolonged irradiation time (i.e. dwell times). The depth and width are also a function of the laser repetition rate (i.e. pulse separation). With progressively lower repetition rates, the laser fluence increases nonlinerly (Appendix A.5). The end result is that at lower laser repetition rates, the micro-via formation on Ti becomes more profound.

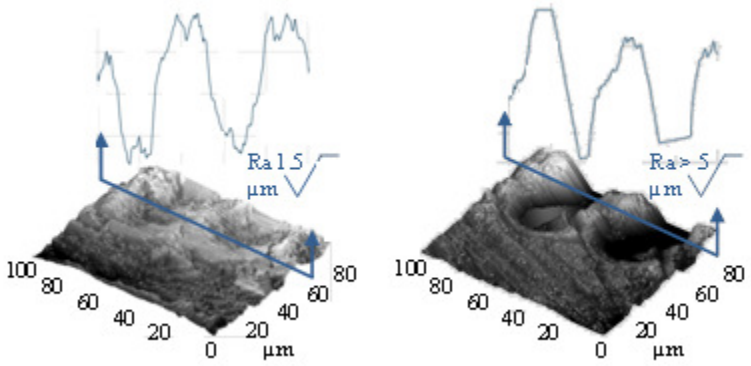

Figure 4.9. Micro-via AFM scans for various 3-D networks (left: high laser repetition and low irradiation time, right: low laser repetition and high irradiation time)

4.4 SUMMARY

Vapour plume condensation is most commonly used to explain nanostructure nucleation within the target plume. Such classical theories should only be used for nucleation mechanism appreciation, not for quantitative analysis of the ambient condition plasma plume. The fsec laser pulses are shorter then heat conduction time scales. Pressure and temperature gradients are mainly a result of plasma formation. As well, multiple pulses are more efficient for plasma generation than a single pulse.

A nanofiber is defined as a single-strand chain of nanoparticles that can be interconnected after a set average of particles which define the overall porosity and promote 3-D network growth under surface ablation conditions. The TiO_2 nanofibers can have tunable porosity by effective webbing effects during the vapour condensation phase. Additionally, these nanofiber networks show anatase and rutile phase compositions which are tunable by laser synthesis parameters.

CHAPTER 5

NANOFIBROUS SERS EFFECT

What happens under SERS is a collective oscillation of plasmons surrounding the atomic lattice. In other words, SERS is dependent on the Localized Surface Plasmon Resonance (LSPR). This phenomenon occurs due to coupling or absorption of incident energy by the conduction band electrons (Figure 5.1). Mathematically, this occurs when the phonon and surface plasmon wave vectors match.[63]

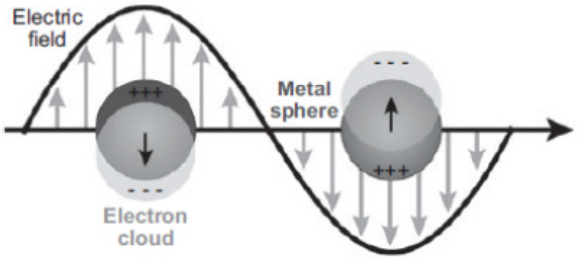

Figure 5.1. LSPR valence electron oscillation by a spherical model[63]

Only two noble metals (i.e. Au, Ag) may traditionally provide large Raman enhancements. As a result, SERS is a highly active area of research. The most effective method for enhancing the Raman spectra involves increasing surface electromagnetism (EM) activity. The EM enhancement is typically from 10^4 to 10^{12}.[64] Optimized enhancement may be realized by varying nanoparticle alloys, nanostructure morphology, density and/or cluster.[65]

5.1 RAMAN ANALYSIS

The low Ti Raman activity, as seen by its broad peak in Figure 5.2, is explained by de-phasing of the surface wave vectors.[66] The Raman active D_{4h} symmetry modes of rutile TiO_2 were detected as B_{1g} (144), E_g (443), A_{1g} (611) and B_{2g} (825) cm^{-1}.[38] Peak shifting was not observed

in these sets of experiments. In addition, the strong 241 cm^{-1} mode is commonly reported but its origin remains disputed. This mode will be briefly considered and investigated along with lower intensity Raman modes at 349 and 710 cm^{-1} in future research.

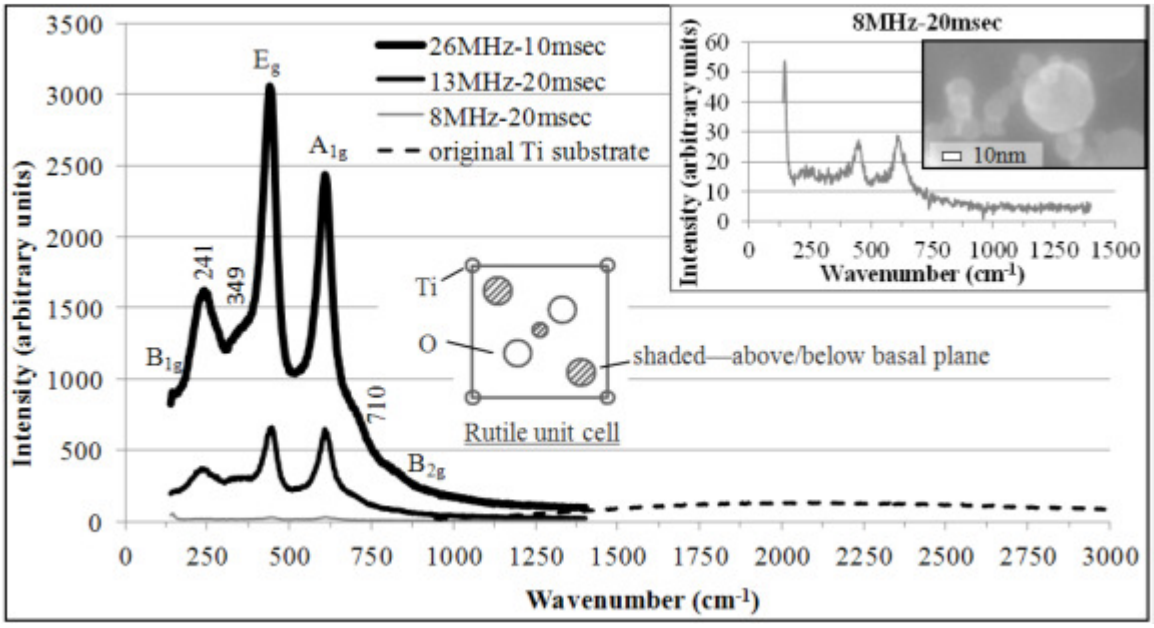

Figure 5.2. Raman spectra of three chosen substrates synthesized by a pulsed femtosecond laser (26 MHz – 10 msec, 13 MHz – 20 msec, 8 MHz – 20 msec) and compared to the original Ti substrate

The power of Raman scattered energy (P_{RS}) is proportional to the Raman scattering cross section (σ^R) and the incident laser beam intensity (I_L):[67]

$$P_{RS} \propto \sigma^R I_L \qquad \text{Eq. 5.1}$$

Since the laser intensity was kept the same throughout all experiments, there must be a significant change occurring with σ^R that results in the scattering intensity increase of Figure 5.2. This intensity change can also be attributed to the enhancement of the Raman spectra and hence the phenomenon of SERS.

For various nano-Ag and nano-Au substrate preparation methods, Raman EF values on the order of 10^5-10^6 are common.[68][69][70][71] Higher enhancement is typically claimed as a result of EM computer simulations. Choi et al., 2010 have shown that such calculations, even for the most ordered substrates, can mislead the EF value by up to two orders of magnitude.[72] The more conservative analytical EF value for the 3-D TiO_2 nanofibrous network was determined to be $1.3x10^6$ (Appendix A.4). It is clear that the TiO_2 nanofiber matrix provides a highly competitive EM enhancement to the most popular Ag and Au substrates. Nonetheless, it is also observed that not all of the nanofiber networks yield high Raman performance. The EM activity of the TiO_2 3-D nanofiber network will be examined next.

5.2 EM ENHANCEMENT MECHANISMS

Transition metals in general have a different electron distribution which becomes difficult to resonate. Consequently, metals like Ti require sophisticated nanofabrication techniques to activate SERS. The nanofibrous network properties as related to plasmon resonance in TiO_2 will be investigated.

The laser frequency that produces the highest plasmon resonance for bulk Ag is in the near-ultraviolet region (UVA) of the EM spectrum.[73] However, research groups commonly use varying wavelengths from 514 nm to 785 nm.[74] This is due from a practical point of view to avoid laser induced molecular degradation. However, However, rutile TiO_2 has plasmon resonance that is in vacuum-ultraviolet (VUV) in addition to being highly damped. [75] For the first time, we demonstrate how rutile TiO_2 in a 3-D nanofiber network could still compare to the EM enhancement of Ag and Au at a laser excitation wavelength as long as 532 nm.

There are three fundamental contributors to SERS: plasmon resonance, charge-transfer resonance and molecular resonance.[73] In this case, plasmon resonance will be studied as

related to substrate self-enhancement. First of all, maximum plasmon resonance occurs between the laser excitation and the Stokes shifted wavelengths.[63] Red-shifting of rutile TiO_2 plasmon resonance from VUV [75] to the 514 nm laser excitation as well as improvement in its dielectric properties is done collectively by the 3-D TiO_2 nanofiber network (Figure 5.3). Tuning of the overall EM enhancement is discussed next.

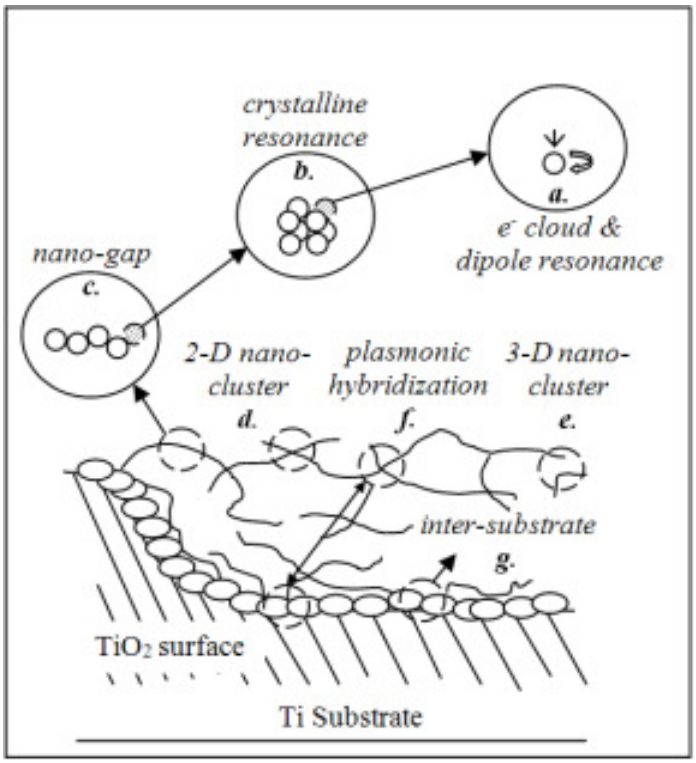

Figure 5.3. A model of the SERS nanofibrous network mechanisms, the scribbled lines represent the 3-D TiO_2 nanofibrous network

Firstly, consider the electron cloud and dipole resonance (Figure 5.3a). The conduction band electrons drive Raman enhancement.[64] However, transition metals (such as Ti) have a relatively poor definition of free electrons due to their electronic structures. In particular, the 3d, 4d and 5d shells are interrelated with the 4s, 5s and 6s shells. This disadvantage is also characterized by high values of dielectric damping which further reduces the EM

enhancement.[76] Small dielectric damping of Ag is what made it the most popular SERS substrate.

Continued laser irradiation reduces the rutile nanoparticle size. When the diameter reduces below 100 nm, radiative damping becomes insignificant and the plasmon bandwidth narrows.[77] Therefore, such improvement of the dielectric function will also improve dipole resonance and hence EM enhancement.

Crystalline resonance (Figure 5.3b) can also affect Raman scattering intensity in the form crystalline order degree. Lattice group and atomic oscillations of TiO_2 are responsible only for the Stokes shifted energy. The scattering intensity is also related to the force constants involved and directly reduces as more O atoms begin to oscillate tangentially to Ti (i.e. two for B_{2g} and four atoms for B_{1g}).[39]

Additionally, selection rules based on linked nanofiber rutile particles can split degenerative modes.[78] From Figure 5.2, this would explain the origin of the 241 cm^{-1} peak since the E_g mode is degenerate.[39] The important aspect to note here is that this new mode is the second highest contributor to the EM enhancement next to E_g itself. From Figure 5.2, the mode-specific Raman scattering intensity enhancements are 16 (B_{1g}), 95 (241cm^{-1}), 117 (E_g), 84 (A_{1g}) and 59 (B_{2g}).

The nanogap (Figure 5.3c) is perhaps the most profound SERS contributor. It was shown that Au-Ag core-shell two particle clusters perform better than Au-Ag monomer alloy particles.[79] A new idea of nanogap “hot spots” emerges.[80] It was shown that a reduction in gap distance at a fraction of one nanometer has almost an order of magnitude amplification for SERS.[72] Figure 5.4 shows that the nanogap between the rutile nanofiber particles is on the order of one

nanometer. Although the nanofiber morphology is similar between synthesis parameters, the 3-D network density changes as in Figure 4.1.

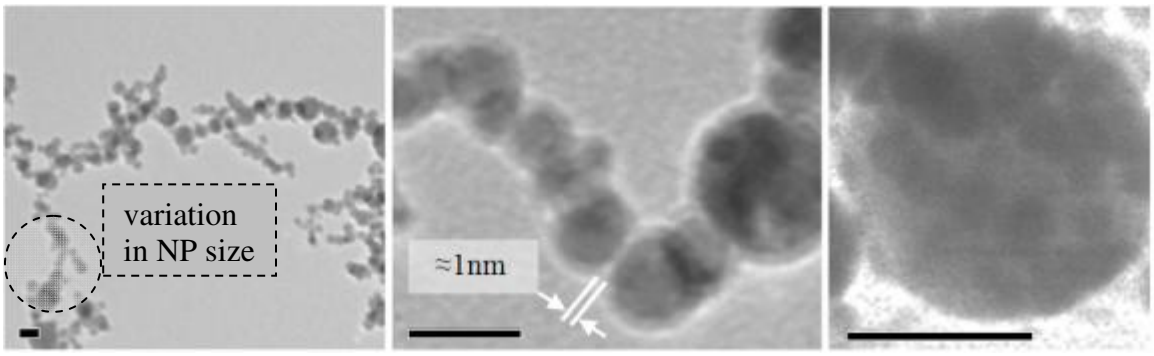

Figure 5.4. TEM of segregated TiO_2 nanofibers. Inset bar scale is 25 nm. The particle shell (middle image) is due to TEM contamination and grows with exposure time

SERS activity of a metal away from its resonant excitation frequency is also contributed by the nanogap.[73] In particular, the dipole plasmon resonance was found to red-shift with reducing nanogaps.[81] These contributions help explain the strong TiO_2 EM enhancement with a 532 nm excitation wavelength.

Nanoclusters improve the overall SERS activity (Figure 5.3d,e).[82] In particular, variations of in-line and spherical nanofiber particles (Figure 5.4) exhibit the “nanolens” plasmon mode coupling effect.[83] The unique characteristic of a “nanolens” is multiplicative multi-stage enhancement which can progress along the nanofiber.[84] Additionally, the nanofibers appear to extend from the TEM grid as seen by partial and complete particle overlapping. This characteristic will extend the “nanolens” effect into the depth dimension of the network.

Reflectivity measurements have revealed that the TiO_2 nanofibrous network has a tunable spectrum response. The maximum intensity peak increases as it varies from 381 – 457 nm. The variation was found to occur by modifying the synthesis pulse repetition rate.[85] Firstly,

increasing intensity is favorable to reduce Stokes shifted light interference which influences the EM enhancement magnitude.[86] Secondly the nanofibrous network can induce refractive index changes to excite further surface plasmons.[87] Thirdly, plasmon width and red-shifting are sensitive to the size of nanofiber particle clusters.[81] In this case, these observations suggest a need to determine the optimum 3-D nanonetwork depth and porosity. This is a design evaluation aspect under ongoing investigation (Appendix A.6).

An additional plasmon resonance red-shift is observed with increasing nanofiber length.[81] The 3-D nanonetwork exploits this phenomenon by having tunable surface (i.e. 2-D) and depth (i.e. 3-D) nanofiber particle clusters (Figure 4.1). A further investigation into extinction efficiency also reveals that it is possible to gain larger EM enhancement at a surface location other than the polarization direction for larger nanoparticles.[77]

Ye et al. have demonstrated that separating gold-nano rings from the gold film by a 50 nm SiO_2 layer led to a three time larger enhancement than placing them directly on the gold film (Figure 5.5).[88] Hatab et al. demonstrated this phenomenon by lithographically patterned Si holding Au nanoantennas.[89] Such phenomenon is also witnessed from Figure 5.2 as scattering intensity varies significantly between different network depths. Such demonstrations suggest plasmon hybridization between the localized surface plasmon (LSP) of the nanostructure and the delocalized surface plasmon (DSP) of the substrate.

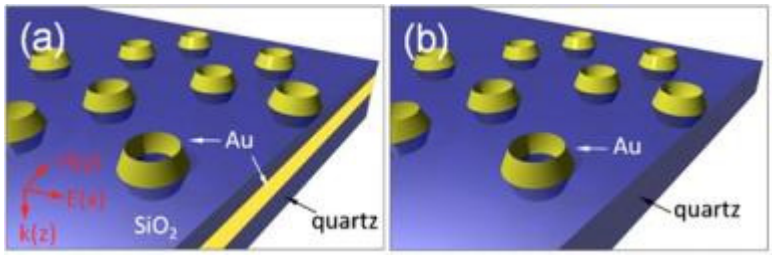

Figure 5.5. Plasmonic hybridization demonstrated [88]

In this case, hybridization occurs between a self-supported rutile TiO_2 nanofiber network on top of the Ti substrate (Figure 5.3f). AFM contact studies were carried out to investigate the nanonetwork physical behavior (Figure 4.7). In comparison to the SEM images, the respective AFM images remain relatively the same regardless of the 3-D nanofiber network. One notable change is how the sharp edges within the periphery of the irradiation center are smooth in the AFM scans. The AFM tip curvature is only up to 10 nm. It is therefore more reasonable to attribute the smoothing of scans to nanofibers being lodged in the crevices by the scanning probe. Once the TiO_2 nanofiber network density increases, there is significantly more AFM scanning interference. This is indicated with white smudges, where white represents a higher elevation with respect to the white-black scale. Although the AFM scans may reveal areas of more dense nanofibers, the scans did not reveal the surface morphology of the network. Therefore, observations consistently suggest that the 3-D TiO_2 nanonetwork is highly flexible and mobile.

The 3-D TiO_2 nanofiber network under layer imaging was demonstrated to be possible in the discussion of Figure 4.7. Higher resolution scans revealed cauliflower-like patterns (Figure 4.7 AFM inset). In this case, 3D-FDTD (Three-Dimensional Finite Difference Time Domain) simulations have shown enhancement at the apex of the spheres and in the crevices when modeled as a plane grating.[76] In general, the coupling effect between small semi-spheres affect incident energy enhancement. As a result, the morphology below the nanofibers is also critical in SERS. All of the aforementioned mechanisms collectively balance to make the 26MHz -10msec TiO_2 substrate exhibit the best SERS performance under the 532 nm excitation.

5.3 SUMMARY

Conduction band electron resonance is responsible for the majority of SERS activity. This is a disadvantage of TiO_2, hence its neglect in Raman sensing developments to date. Nanofibrous TiO_2 SERS response is evident from significant signal intensity increase. The combination of EM mechanisms is argued to collectively stimulate SERS. The nanoparticle architecture of the nanofibers is a significant contributor to SERS. It features a collective contribution from highly effective nanoparticle EM phenomenon such as the nanogap, nanocluster and plasmonic red-shifting. Additionally, the 3-D nanofibrous network has an optimum depth. The depth component contributes to plasmonic hybridization, 3-D nanoclustering and nanolens effects.

CHAPTER 6

RAMAN MOLECULAR DETECTION

Raman vibrational spectroscopy provides insightful characterization of probed substances by unique Stokes-shifted frequencies.[65] SERS greatly improves the sensitivity of traditional Raman spectroscopy while reducing the laser power and collection time. This has allowed for extensive chemical and bio-sensing applications including rapid sensing of Anthrax,[22] detection of specific DNA sequences,[84] cell mapping[90] and single molecule detection.[91] Crystal violet is a common probe molecule for SERS studies due to its large Raman scattering cross section (Eq. 5.1).

Bisphenol A (BPA) is a common polycarbonate (PC) monomer. Krishnan et al. (1993) discovered that BPA can be released from PC products during autoclaving and then dissolve into the surrounding environment.[92] BPA is also a known endocrine disrupter which leads to a disturbed hormone balance in humans.[93] Diclofenac sodium (DSS) is a non-steroidal and anti-inflammatory pharmaceutical ingredient. However, DSS is also amongst the most commonly detected pharmaceutically active compounds in ground and surface water.[94] Since chemical adsorption may be specific to certain human organs, it is important to have analytical capacity for molecular level identification and adsorption analysis of these aromatic compounds in environmental samples.

6.1 CRYSTAL VIOLET DYE

SERS activity, sensing reproducibility and substrate signal are important factors when designing a practical sensor.[65] Inherently, homogeneous nucleation will generate a distribution of nanoparticle sizes—and in this case—also a variation in network porosity. Crystal violet (CV) has been applied to study potential analyte interactions. Firstly, Figure 6.1 clearly demonstrates

SERS due to the 3-D TiO_2 nanofiber network. Physisorption is also indicated by the phenyl-N stretch peak shift to 1377 cm^{-1}.[95] Secondly, the 26 MHz – 15msec TiO_2 substrate was found to reveal the best CV spectra as opposed to 26 MHz – 10msec from Figure 5.2. A longer synthesis time (i.e. more effective laser pulses) creates a denser network (Figure 4.1) which can aid in nanofibrer stability. This is especially important liquid solution analysis. Additionally, adsorption kinetics may differ between the TiO_2 nanofibrous networks. Therefore, it is necessary to tailor the 3-D TiO_2 network towards favorable detection of a particular molecule.

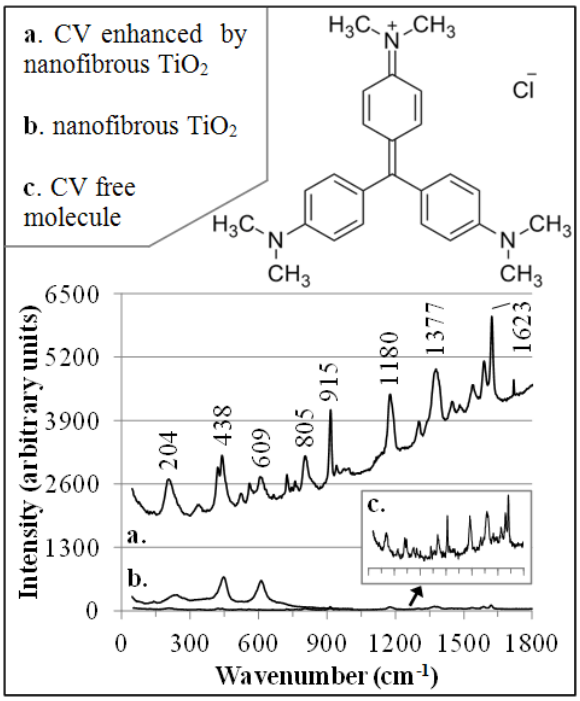

Figure 6.1. CV-TiO_2 Raman spectra enhancement using a 26 MHz -15 msec substrate (a. CV enhanced by nanofibrous TiO_2, b. nanofibrous TiO_2, c. CV free molecule)

Thirdly, the 241cm^{-1}, 443 (E_g), 611 (A_{1g}) and 825 cm^{-1} (B_{2g}) TiO_2 peaks appear quenched by the carbon-nitrogen-carbon bending and out-of-plane deformations of CV at 204, 438, 609 and 805 cm^{-1}.[95] Nonetheless, minimal CV peak shifting was observed for these modes (up to 2 cm^{-1}). Such behavior was seen previously by Musumeci et al. and attributed to charge transfer

complex formation.[96] But contrary to Musumeci, it was demonstrated here that SERS response from TiO_2 is not limited to the charge transfer phenomenon which otherwise requires harmful near ultraviolet excitation. Complete CV results are summarized under Appendix A.3.

6.2 BISPHENOL-A

Background noise dominates the Raman spectra with a commercial Ti substrate (Appendix A.2). However, the TiO_2 nanofibrous sensor pads exhibit appreciable BPA detection improvement under aqueous conditions (Figure 6.2). BPA features two hydroxyl groups that could potentially compete against dissociated water, especially on rutile TiO_2.[97] BPA conforms to C_{2h} symmetry with 72 irreducible vibration modes. The Raman active A_g and B_g modes reveal ring deformation and in-plane C-H bending behavior.[98] It is difficult to distinguish between ring deformation modes below 660 cm^{-1} due to the overlapping rutile and anatase signals. There was no enhancement of BPA dry residue across all studied sensor pads.

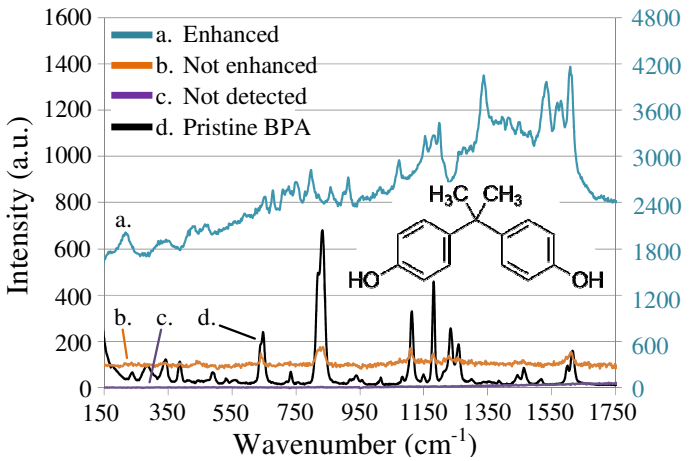

Figure 6.2. Detection of aqueous (aq.) and dry residue (dr.) BPA by various sensor pads (MHz – msec): a. 4 – 1 (aq.), b. 13 – 20 (dr.), c. commercial Ti (aq. or dr.)

6.3 DICLOFENAC SODIUM SALT

As opposed to BPA, DSS was detected better under dry residue conditions given its high solubility under aqueous conditions. DSS structure can have two nonsymmetrical isomers with 58 irreducible vibration modes. It bonds with the lone pair oxygen electrons of the carboxylate group.[99] The band at 1575 cm^{-1} shifted to 1585 cm^{-1} indicating carboxylate orientation to water even after drying. This effect was previously reported by Weerd and Kazarian (2005).[100] However, the stable 1408 cm^{-1} band indicated that there was no dissociation of sodium. This was an expected result as drinking water already contained up to 29.6 mg / L of Na and 39.9 mg / L of Cl^- content which may substantially reduce DSS solubility.[101]

Figure 6.3 demonstrates a gradual improvement in spectra between three TiO_2 sensor pads. The TiO_2 Raman background signal is clearly noticeable with sensor pads b. and c., whereas their intensity is quenched with sensor pad a. as the overall spectra improves. Such phenomenon may be indicative of improved bonding over physisorption.[102] Optimum sensor pads for BPA and DSS under aqueous and dry residue conditions all vary. The point of discussion will be to evaluate what parameters influence such detection compatibility.

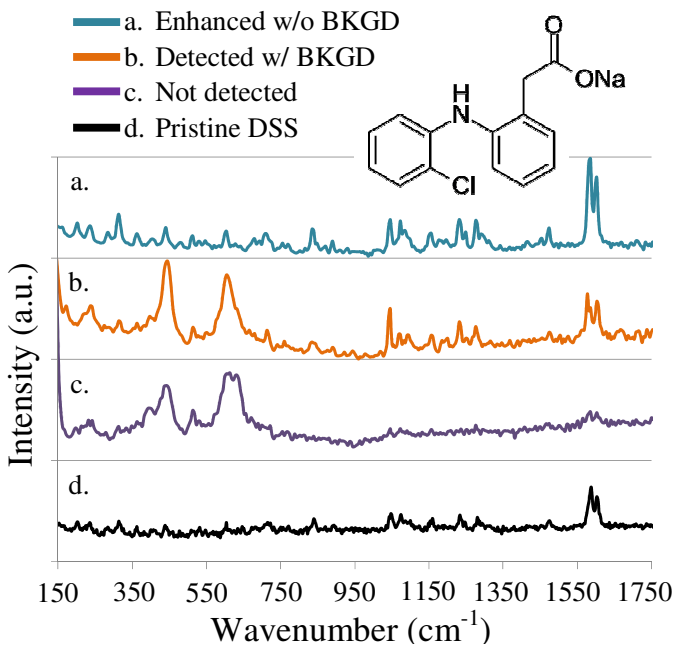

Figure 6.3. Detection of dry residue DSS by various sensor pads (MHz – msec): a. 8 – 15, b. 26 – 15, c. 4 – 25; note: each spectra spans ca. 200 a.u.

6.4 RAMAN DETECTION MAP

Applying an aqueous solution may modify the TiO_2 nanofiborus network architecture. The main concern is particle aggregation. Water is generally chemisorbed on anatase TiO_2 as dissociated hydroxyl groups (OH).[103] Any resulting pH differences can influence repulsive forces between TiO_2 nanoparticles and induce aggregation.[104] Additional aggregation is possible due to the Na, Cl and Cl^- [105] found in the drinking water. Moreover, the anatase to rutile phase mixtures (Figure 4.6) have been discovered after the nanofibrous SERS effect experiments. The resultant anatase to rutile phase mixture synthesis control is yet an undeveloped field of nanofibrous study. All of these combined uncertainties will be discussed by an end-result of Raman detection capacity.

It was previously determined that the minimum TiO_2 nanonetwork generation threshold is 2 MHz (i.e. 500 ns pulse interval) at 1 msec dwell time. A shorter pulse interval promotes a more stable plasma plume while longer dwell times promote 3-D network structuring.[12] These guidelines were adopted for TiO_2 sensor pad development, the results of which are presented by Figure 6.4. The sensor pads were ranked based on the strong 1585 cm^{-1} carboxylic band for DSS and the 1610 cm^{-1} in-plane ring stretch band for BPA. Effects of micro-vias on Raman signal intensity are summarized by Appendix A.2.

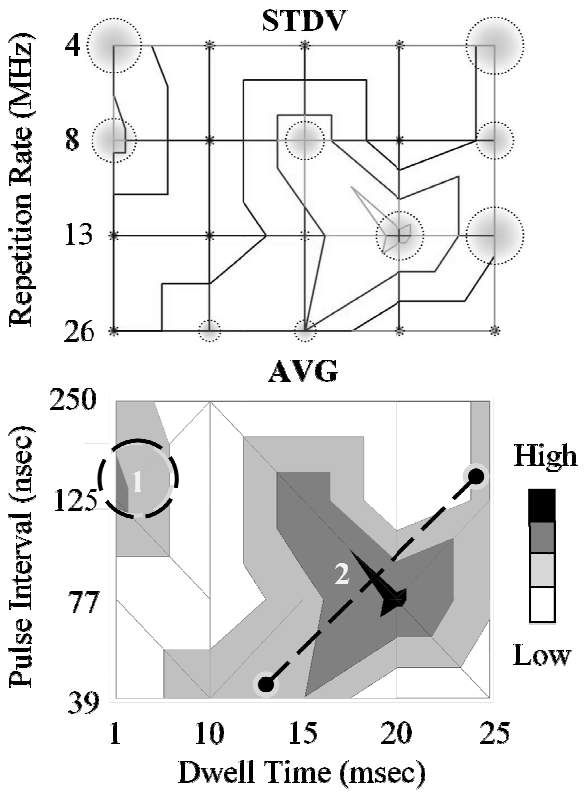

Figure 6.4. Raman detection sensitivity map averaged for all TiO_2 sensor pad experiments and showing standard deviation; pulse interval = 1 / laser repetition rate

There are two major features across all experiments (highlighted within Figure 6.4). Feature 1 exhibits good BPA and DSS detection. At the same time, the relative standard deviation is high

as shown by the large diameter circles of the STDV map. It is usually expected to have variability in Raman response, especially under aqueous conditions.[25] The micro-vias also contribute to reproducibility concerns (Appendix A.2). Nanofiber network contributions will be discussed here.

First of all for feature 1, the sensor pads exhibit variable hydrophilic properties. feature 1 exhibits the most effective surface wetting.[13] Secondly, synthesis fluence is the highest at Feature 1 (Appendix A.5). The plume temperature and pressure properties correspondingly change to increase the anatase TiO_2 nanofiber constituency. Thirdly, increasing the network depth (i.e. longer dwell time) with less stable plume behavior (i.e. longer pulse intervals) tends to result in null detection capacity across BPA and DSS experiments. Therefore, Feature 1 represents a shallow 3-D network with a high anatase to rutile TiO_2 ratio that is highly influenced by surface wetting.

Feature 2 spans a greater detection band. In general, the standard deviation reduces with a lower network depth (i.e. shorter dwell time) and with more stable plume behavior (i.e. shorter pulse intervals). feature 2 is bound by the nanofiber threshold and optimum network porosity. Firstly, the laser fluence at 39 and 77 ns pulse intervals is enough to oxidize the Ti surface but not to generate nanofibrous 3-D networks. Secondly, porosity controls diffusion of analytes in the 3-D nanonetwork and increases the number of metal to analyte contacts.[106] An optimum porosity [107] is related by dwell time and pulse interval parameters which in turn influence sensor stability. Consequently, Feature 2 characterizes a field of parameters with similar resulting 3-D nanofibrous network stabilities.

Surface porosity was further investigated by optical surface roughness. SNOM permits narrow field views of a particular micro-via from a particular TiO_2 3-D nanofiber network. A normalized

roughness construct was developed as G = Sa – Sa / Max, where Sa is the average surface roughness and Max is the maximum surface roughness (Appendix A.5). Figure 6.5 shows that the smoothest substrate was commercial Ti. The next smoothest substrate was generated at 2 MHz – 25 msec (G = -0.0286). This result validates the previous discussion about heavily generated and low porosity networks under relatively unstable plume characteristics. Moreover, the G roughness construct also fully explains the previous apatite precipitation uniformity observations.[13]

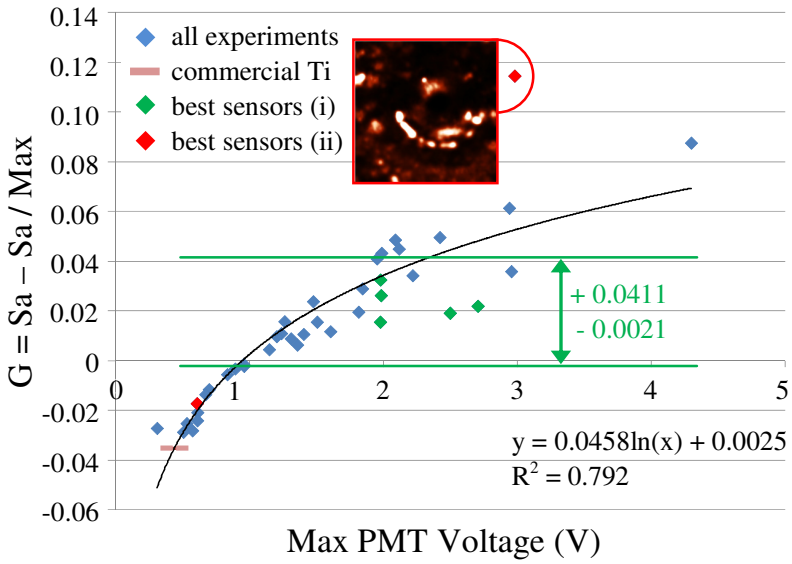

Figure 6.5. Roughness parameter G vs. Max reflection intensity, inset: SNOM scan

Consequently, the 2 MHz – 25 msec sensor pad fell outside the G = -0.0021 to +0.0411 criteria of Figure 6.5. The best sensors (i) were 8 – 1, 8 – 15, 13 – 15, 13 – 20 and 26 – 10 (MHz – msec). Falling outside the G criteria, the best sensors (ii) were 4 – 25 and 26 – 15 (MHz – msec). The 26 – 15 sensor pad was in the highly rough region and may have affected the SNOM scanning probe. However, the 4 – 25 sensor pad was in the smoother region and preferred the detection of BPA dry residue. There may be other phenomenon occurring such as TiO_2 phase

mixtures and 3-D network stability as discussed earlier. Nonetheless, the current G construct predicts an optimum interface roughness of the 3-D TiO_2 nanofibrous networks.

6.5 SUMMARY

Detection with CV clearly demonstrated the SERS phenomenon that was previously predicted by the nanofibrous SERS effect. Detection of BPA was preferable only under aqueous conditions. This was attributed to better dispersion for easier hydroxyl group bonding to the TiO_2 surface. Detection of DSS was preferable mainly under dry residue conditions. This was attributed to the higher solubility of DSS. There was no dissociation of Na from DSS. Raman spectra has shown various levels of TiO_2 background, the relative reduction of which resulted in a better defined and higher intensity DSS spectra. DSS and BPA detection schemes for dry and aqueous conditions were combined into a Raman detection map. This was done to more equally compare Raman results without specific knowledge of aggregation affects due to drinking water and involved solvents.

The Raman detection map reveals two main features. Feature 1 represents a shallow 3-D network with a high anatase to rutile TiO_2 ratio that is highly influenced by surface wetting. Feature 2 characterizes a field of parameters with similar resulting 3-D nanofibrous network stabilities. SNOM reflection studies were carried out to verify the preference of smooth and uniform networks to detection of BPA and DSS.

CHAPTER 7

CONCLUSION AND RECOMMENDATIONS

A unique nanosynthesis method using a femtosecond laser was used to generate crystalline TiO_2 nanofibers from a Ti substrate under ambient conditions. Vapour plume condensation is most commonly used to explain nanostructure nucleation within the target plume. The resultant nanofibers were defined as a single-strand chain of nanoparticles that can be interconnected after a set average of particles which define the overall porosity. The network constituency was tunable by synthesis parameters between dominantly rutile phase to a mixture of rutile and anatase. Phase control and synthesis mechanics have yet to be studied.

When electromagnetic energy interacts with a molecule, there is possibility that the energy will be scattered. It was shown that the level and the shift of scattered energy are unique to molecular vibrations and could be characterized by Raman spectroscopy. It was also shown that nanoscale material modification can enhance the power of this scattered energy for molecular sensing purposes. The resulting Raman enhancement mechanisms feature nanogap, nanocluster and plasmonic hybridization. The appreciable $1.3x10^6$ relative enhancement of TiO_2 supports a method to prepare SERS active substrates from traditionally inactive materials. SERS activity was confirmed using a CV dye.

Raman detection of aromatic BPA and DSS in drinking water was found to be sensitive with variations in network depth, surface morphological uniformity and sensor porosity. A generalized detection map was developed which showed a strong favorability towards uniform and porous TiO_2 nanofibrous 3-D networks. In addition to making the chemical and physical favorability of TiO_2 viable for Raman spectroscopy, this study has developed a unique nanoarchitecture for chemical sensing and bio-molecular detection.

Further optimization is needed towards product commercialization in the chemical and bio-molecular sensor industries. Since it was found that the nanofibrous network has various degrees of performance dependant on the chemical type and state, further testing may be necessary before marketing the sensor for chemicals other than CV, BPA and DSS. One possible preliminary solution is to choose the highest average performing substrates from Figure 6.4 that also demonstrated the least standard deviation (as represented by smaller diameter circles). If Raman performance is unsatisfactory, higher standard deviation substrates may be experimented tested. It may be that the particular analyte has a highly specific SERS condition hence the higher standard deviation as not all analytes are compatible with that particular TiO_2 nanofibrous network.

APPENDICES

A.1 DRINKING WATER ANALYSIS

Table A.1.1 summarizes inorganic elements that have been found to influence SERS response.[108] NaCl is commonly known for aggregation of nanoparticles.[105] Therefore its presence or even ionic dissociation can have an impact.

Table A.1.1. List of inorganic parameters present in Toronto drinking water based on 2011 public data provided by the City of Toronto

	Number of Samples	Number of Detectable Results	Method Detection Limit [mg/L]	Maximum [mg/L]	Minimum [mg/L]	Average [mg/L]
Ag	17	0	0.0001	0.0000	0.0000	0.0000
Al	594	594	0.005	0.339	0.034	0.063
Ca	105	105	0.2	37.3	33.0	34.9
Cl	6014	6014	0.10	2.20	0.25	1.07
Cl^-	88	88	0.2	39.9	23.8	26.5
Cu	17	7	0.001	0.024	0.000	0.002
Fe	16	11	0.004	0.015	0.000	0.005
Na	159	159	0.4	29.6	12.6	14.4

Generally, SERS intensity and background noise reduction is attainable by using dyes with large Raman scattering cross-sections such as Rhodamine 6G (R6G) and crystal violet (CV),[109] however which are also known pollutants.[66] Therefore, in the interest of

sustainability as well as unambiguous characterization of adsorbent interactions with the TiO_2 3-D nanofibrous network, no dyes were used in this study.

A.2 RAMAN, AFM AND SNOM DATA

Water has a small Raman cross section and hence does not severely interfere with measurements in aqueous environments.[110] Figure A.1.1 also shows that neither BPA nor DSS could be detected on a plain Ti substrate. SERS of the TiO_2 3-D nanofibrous network is discussed in detail within the with Raman molecular Detection.

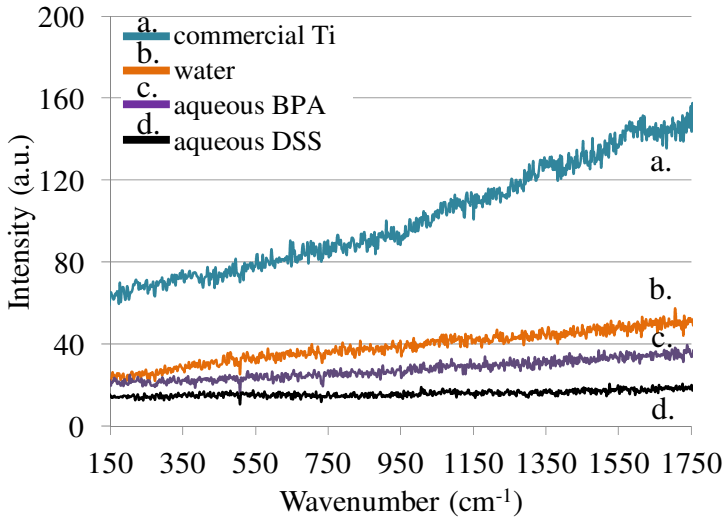

Figure A.1.1. Raman signal under aqueous conditions dominated by background noise when using a commercial Ti substrate

The TiO_2 nanofibrous sensor pad was prepared with micro-vias 50 µm apart so that the generated features would just begin to overlap and accumulate. The Raman degree of focus (DOF) is also an important consideration in analyzing the TiO_2 3-D network. A 100x objective would have a DOF of ca. 1 – 2 µm. However, AFM scans revealed possible network depths of

greater than 5 µm. Although background noise is greater with 50x, the DOF is ca. 10 µm so the entire network thickness could be sampled.

Figure 4.1 SEM scans show that the nanofibrous porosity spans the entire sensor pad surface. However, the structure of the 3-D TiO_2 network within the micro-vias is yet unclear. It appears that there may be no nanofibrous structure within the micro-vias. The Raman microscope was equipped with a camera and a micrometer stage hence it was possible to position the focus on the inter- and intra-via sensor pad areas. Figure A.2.2 shows that the Raman signal drops when the Raman laser is positioned over the micro-via. The signal drops significantly when the via depth and width increase. This effect is dominant at lower laser repetition rates (i.e. longer pulse separation).[11]

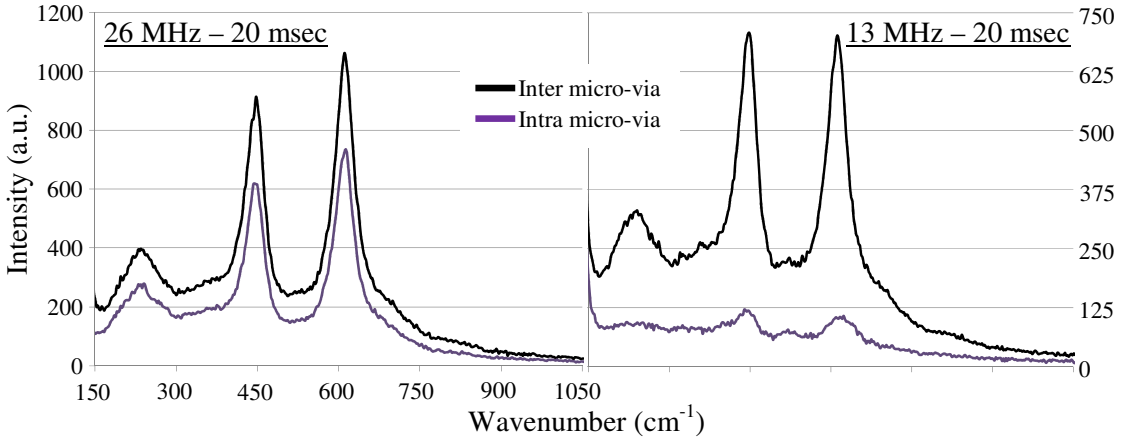

Figure A.2.2. Micro-via contribution to Raman signal

Singular micro-vias were synthesized 250 µm apart under different laser parameters for scanning near field optical microscopy (SNOM) reflection studies. SNOM graphical data was analyzed with built-in SNOM Nova 1.1 software. Average roughness was computed by Nova under ISO 4287/1. The SNOM sample stage had a micrometer adjustment that enabled precise maneuverability between micro-via centers. Figure A.2.3 summarizes maximum normalized

registered photomultiplier module (PMT) voltage. Firstly, scans that appear darker overall have higher localized intensity points. Secondly, Figure A.2.3 shows that the micro-via's ridges are typically the most intense since the ridges are closer to the scanning probe. Overall, sources of error may include SNOM micro-via positioning between scans, scanning probe damage and/or environmental factors such as acoustics. No chemicals were used with SNOM trials.

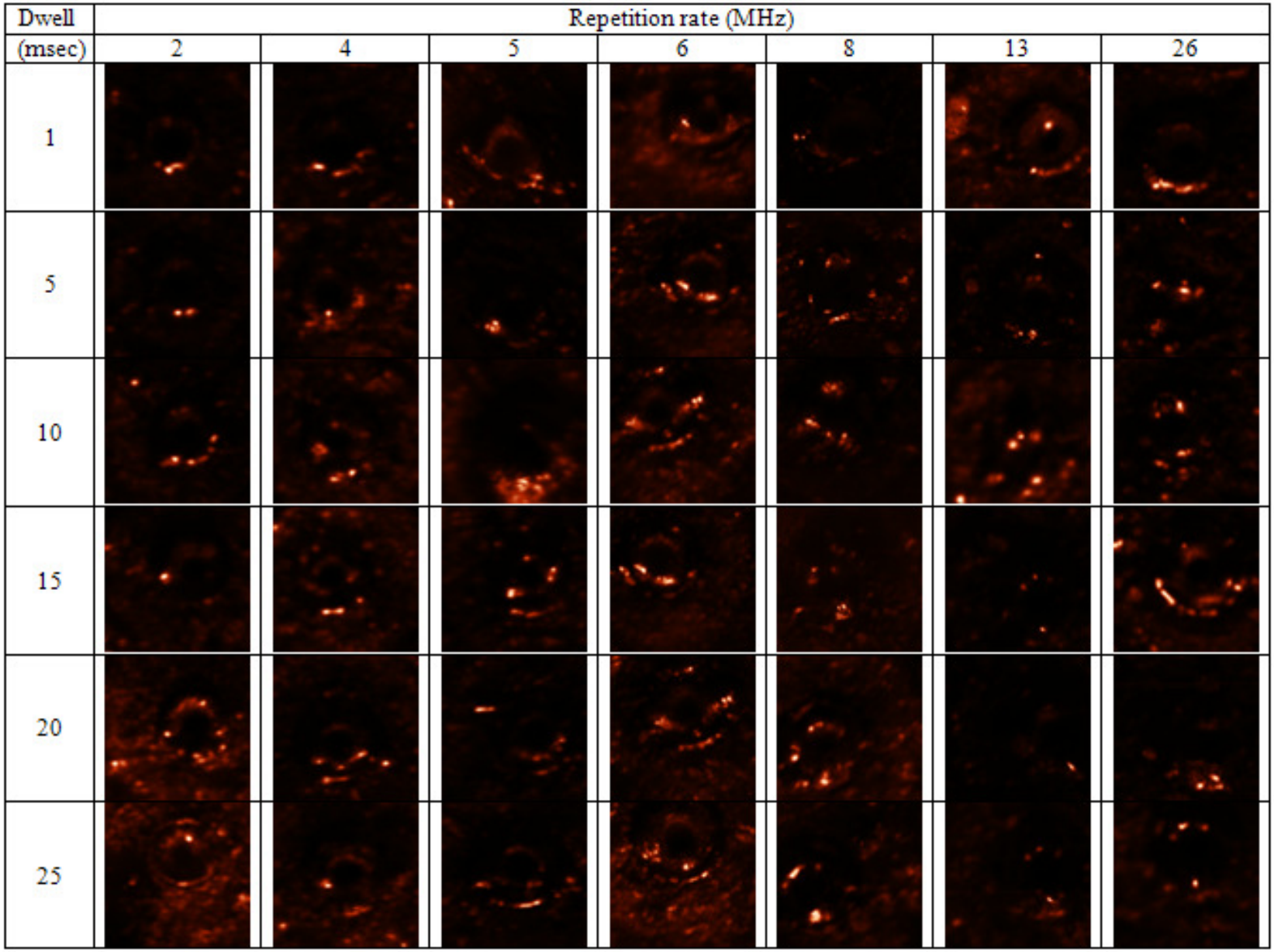

Figure A.2.3. SNOM reflection map for different sensor pads, the irradiated spot is ca. in the center; scan window is 100x100 µm

A.3 COMPLETE CRYSTAL VIOLET DYE EXPERIMENTS

Raman spectroscopy is not currently a standardized method for molecular detection. The first step was therefore to determine the appropriate exposure time, power and edge filter settings. Figure A.3.1 demonstrates the importance of choosing a proper exposure time and power.

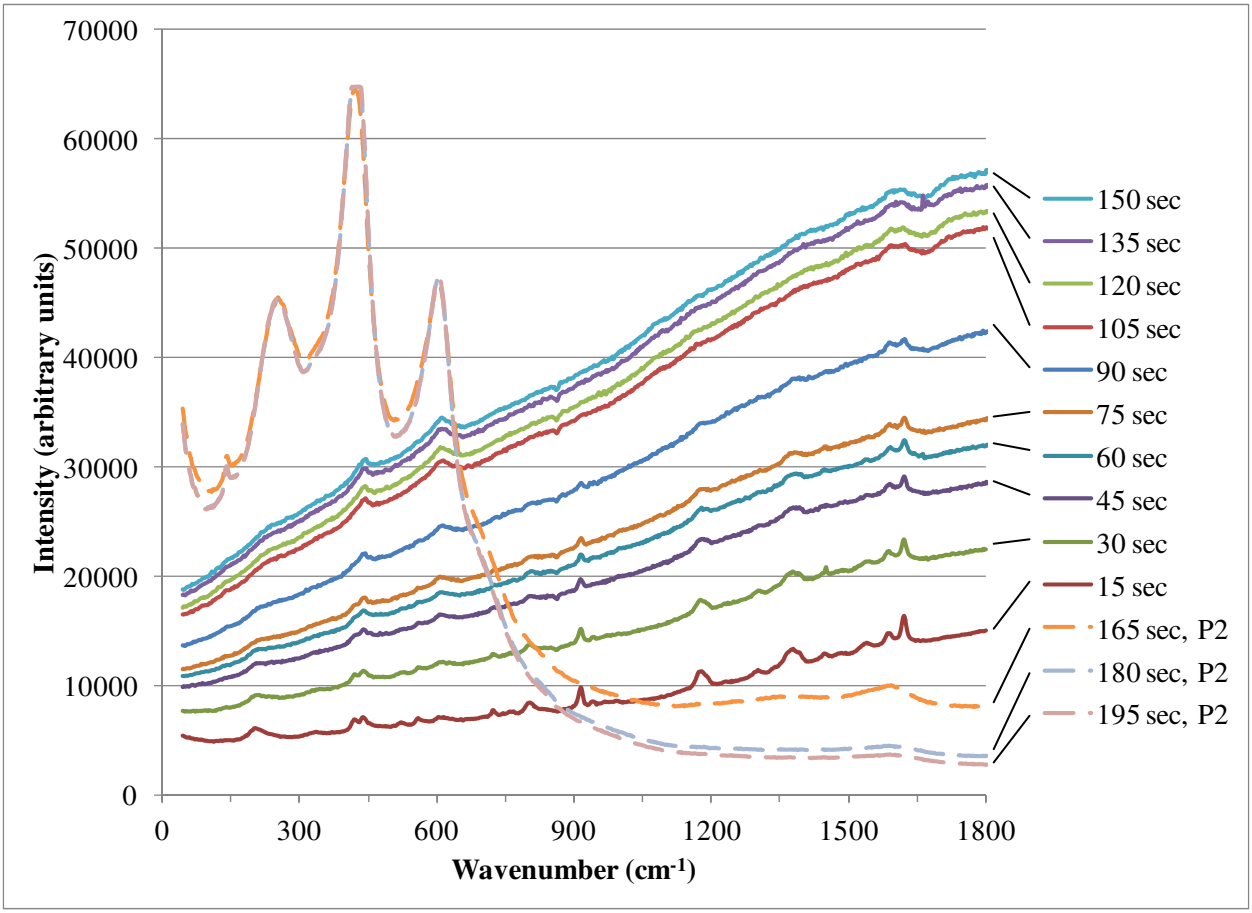

Figure A.3.1. Degradation summary of the CV dye with continuous exposure when using the 26 MHz -15 msec TiO_2 substrate. P2 represents increased power from 1 mW to 79 mW by changing the laser filter attenuation

At first, Figure A.3.1 shows a fair response at 15 sec (i.e. 5 sec exposure time with a three time accumulation) from CV when applied over the nanofibrous TiO_2 3-D network. However,

increased exposure time steadily degrades the CV solution. While this occurs, the overall Raman intensity is increasing due to increasing fluorescence. When the power is increased at 165 sec, the rutile TiO_2 spectrum dominates the Raman response. Seeing the unprecedented intensity of these rutile peaks makes it important to also recognize that this procedure may have great potential for further enhancement of the TiO_2 nanofibrous network if the resultant substrate is used for subsequent molecular detection. Once the parameters were chosen, the TiO_2 substrates were tested for CV detection capacity. Figure A.3.2 shows such experimentation results.

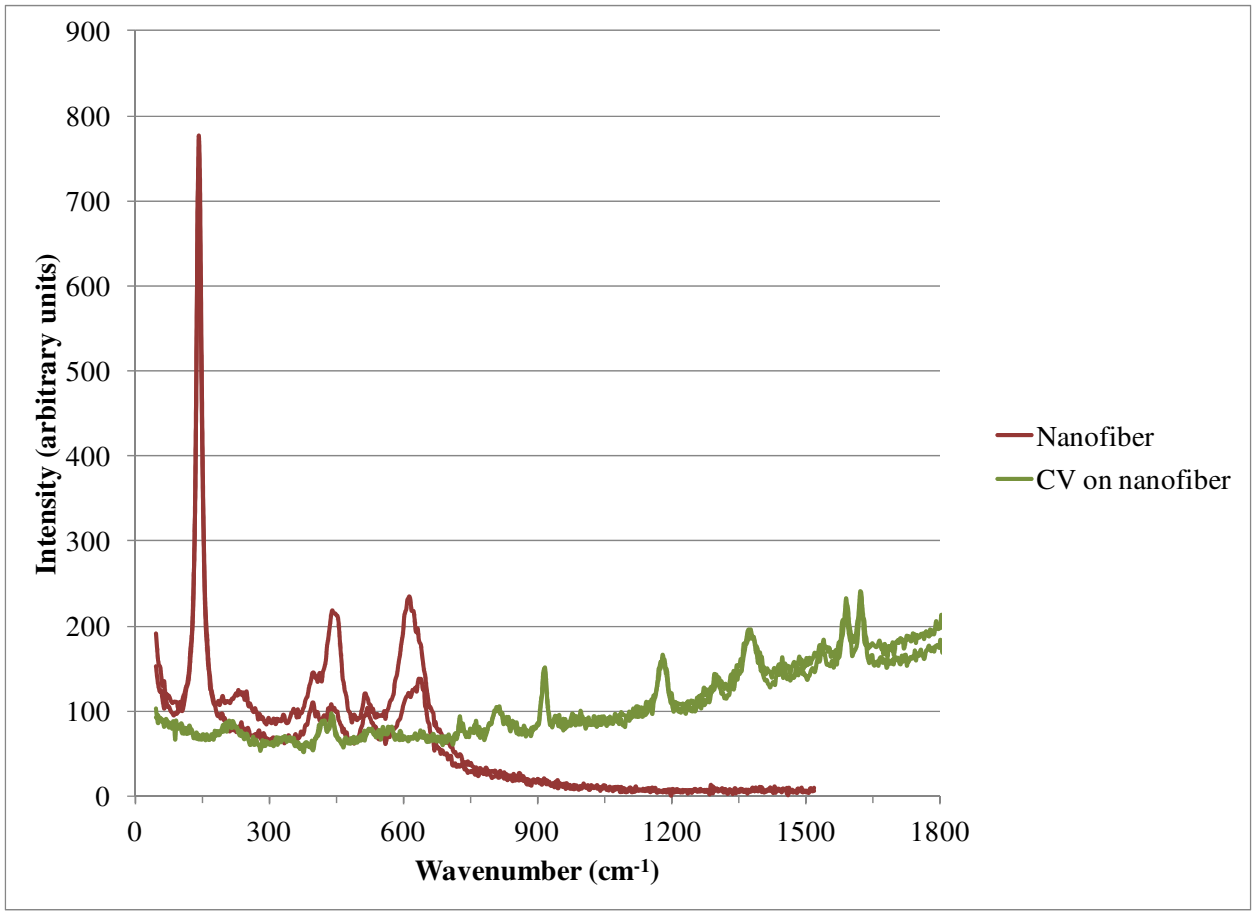

Figure A.3.2. CV-TiO_2 experiments using the 8 MHz -15msec substrate, four spectra are shown

From Figure A.3.2, there is no clear enhancement of the CV dye. In addition, the nanofiber rutile spectra is not clearly defined which indicated the presence of impurities. This affect is more pronounced with Figure A.3.3.

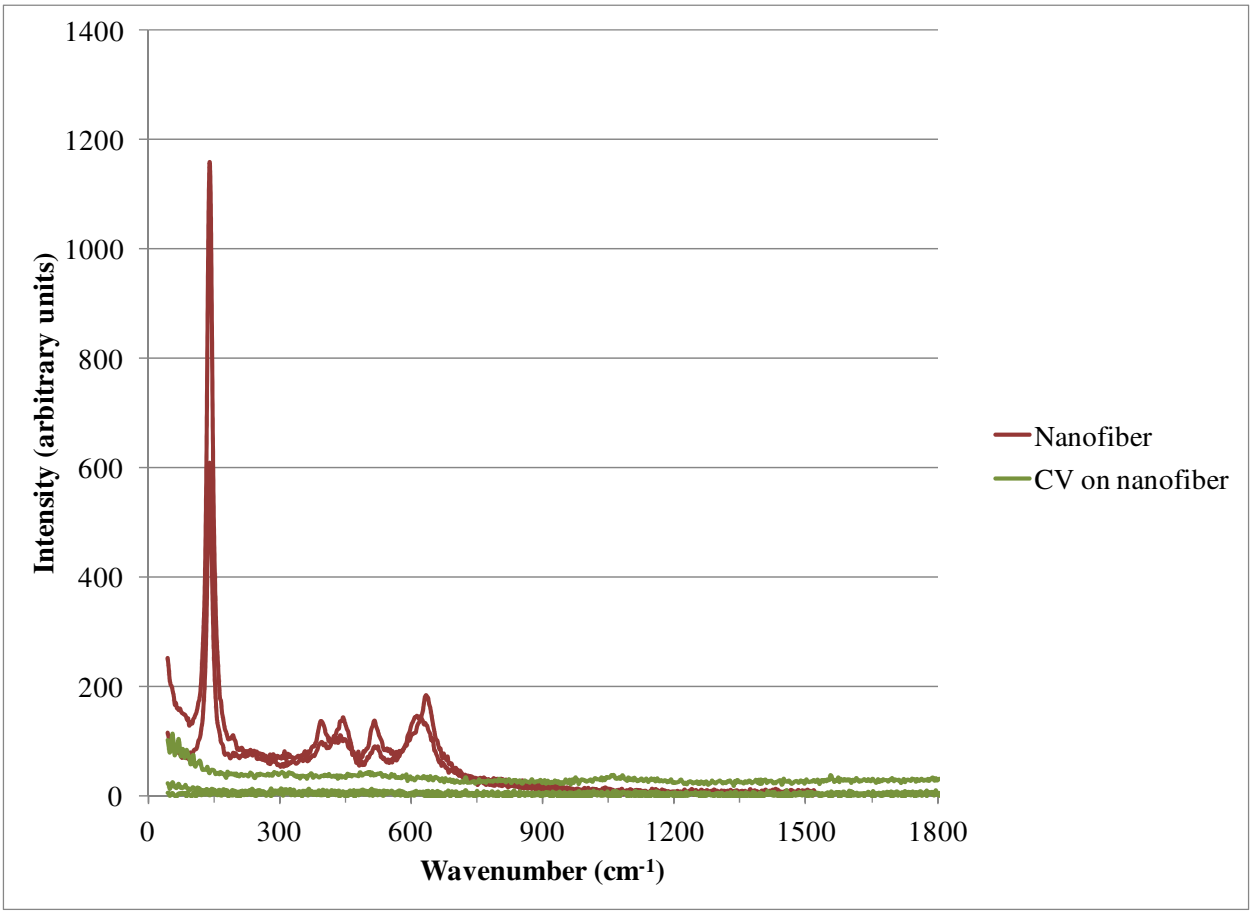

Figure A.3.3. CV-TiO_2 experiments using the 13 MHz -15msec substrate, four spectra are shown

As shown by Figure A.3.3, not only is there no enhancement of the CV dye after application, there is a total loss of Raman response. Firstly, the substrate is no longer pure rutile, as anatase wavenumbers begin to appear. Secondly, the stability of the 3-D network with the CV dye may be lower which could result in excessive aggregation and hence loss of any nanofibrous network advantages. The exact justification for such spectra degradation is still speculative and is subject for a thorough investigation in future research. Nonetheless, the majority of substrates did

provide a clear Raman response. Figure A.3.4 shows the typical experimental result by using the best Raman laser parameters.

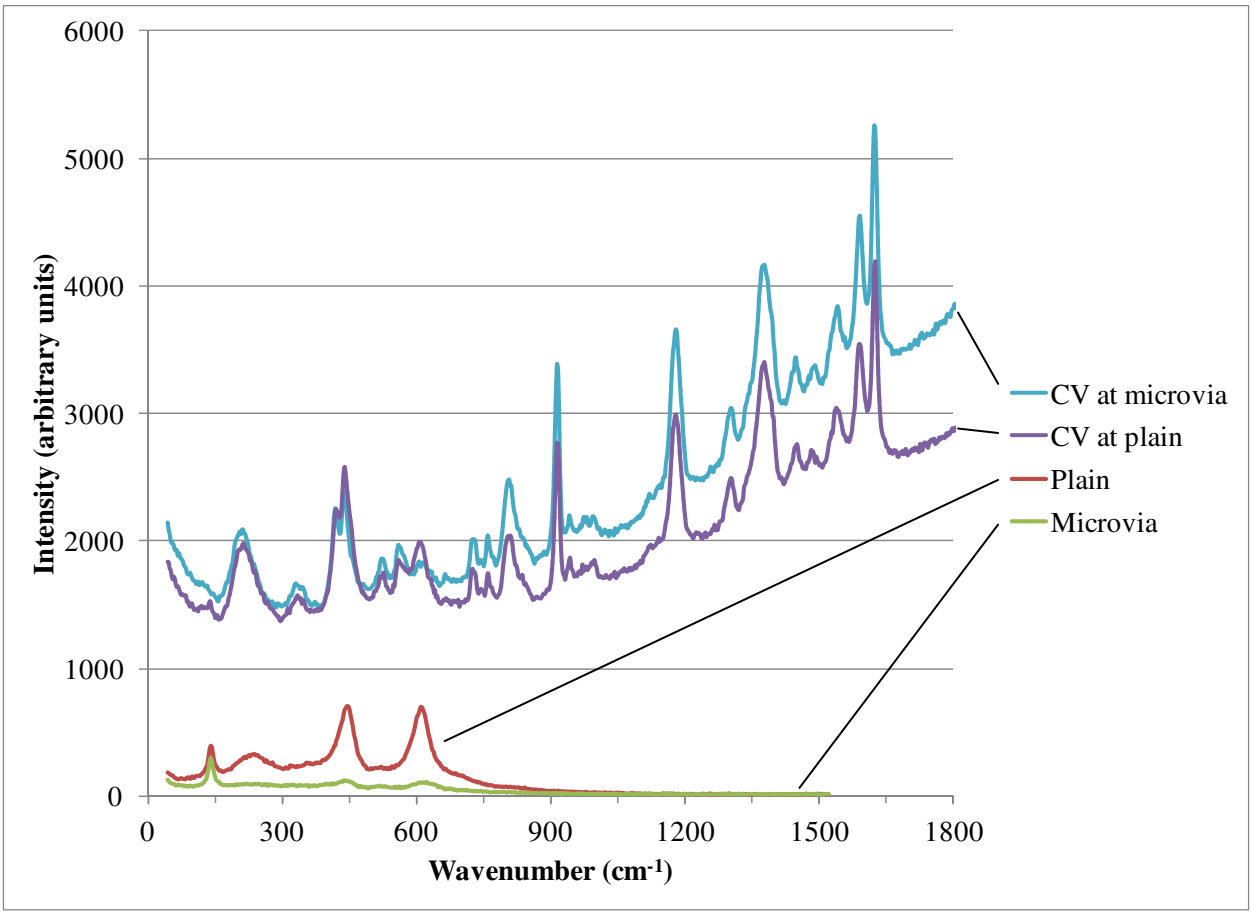

Figure A.3.4. CV-TiO_2 experiments using the 8 MHz -1msec substrate

The Raman sample stage was robotically controlled with micrometer resolution. Together with the built in camera, it was possible to position the Raman laser beam over the microvias or the inter-microvia plains when visible (Figure 4.1). Firstly, Figure A.3.4 demonstrates enhancement of the CV dye as typical CV intensity with the chosen parameters was on average 150 a.u.. Secondly, there is a noticeable drop in intensity of the TiO_2 substrate when the laser is positioned over the microvia. This is an expected result as the microvia depth can draw the laser out of focus. Nonetheless, the importance of nanofibers is demonstrated after applying the CV

dye. Regardless of whether the laser is positioned over the microvias or in between, the intensity remains about the same. Therefore, the nanofibers act as a porous medium to support molecular detection away from the surface. It is also possible to reduce the effect of microvias if desirable as shown by Figure A.3.6 which will be presented later. The highest attained Raman enhancement of the CV dye is shown by Figure A.3.5.

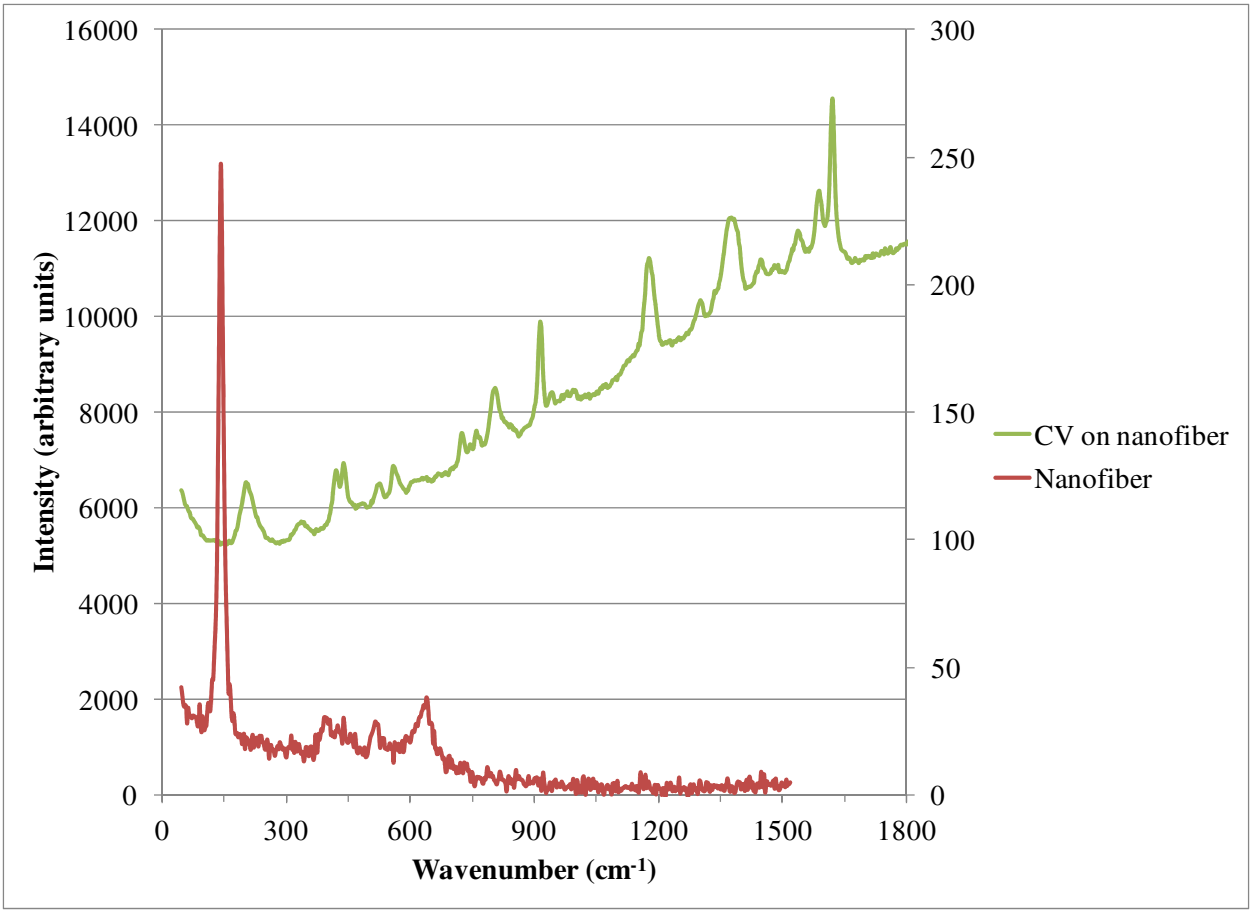

Figure A.3.5. Highest observed enhancement of the CV dye when using the 8 MHz – 20 msec TiO_2 substrate, Nanofiber spectra is on the secondary axis

Following the calculation procedure of Appendix A.4, the calculated EF of Figure A.3.5 is 3.1×10^{-6}. However, the rutile nanofiber spectrum once again shows impurities as was seen with Figure A.3.2 and Figure A.3.3. This is an interesting result as such behavior typically results in

null spectrum response or at best no enhancement. We chose to present the most consistent enhancement data, as summarized by Figure A.3.6 and showcased by Figure 6.1.

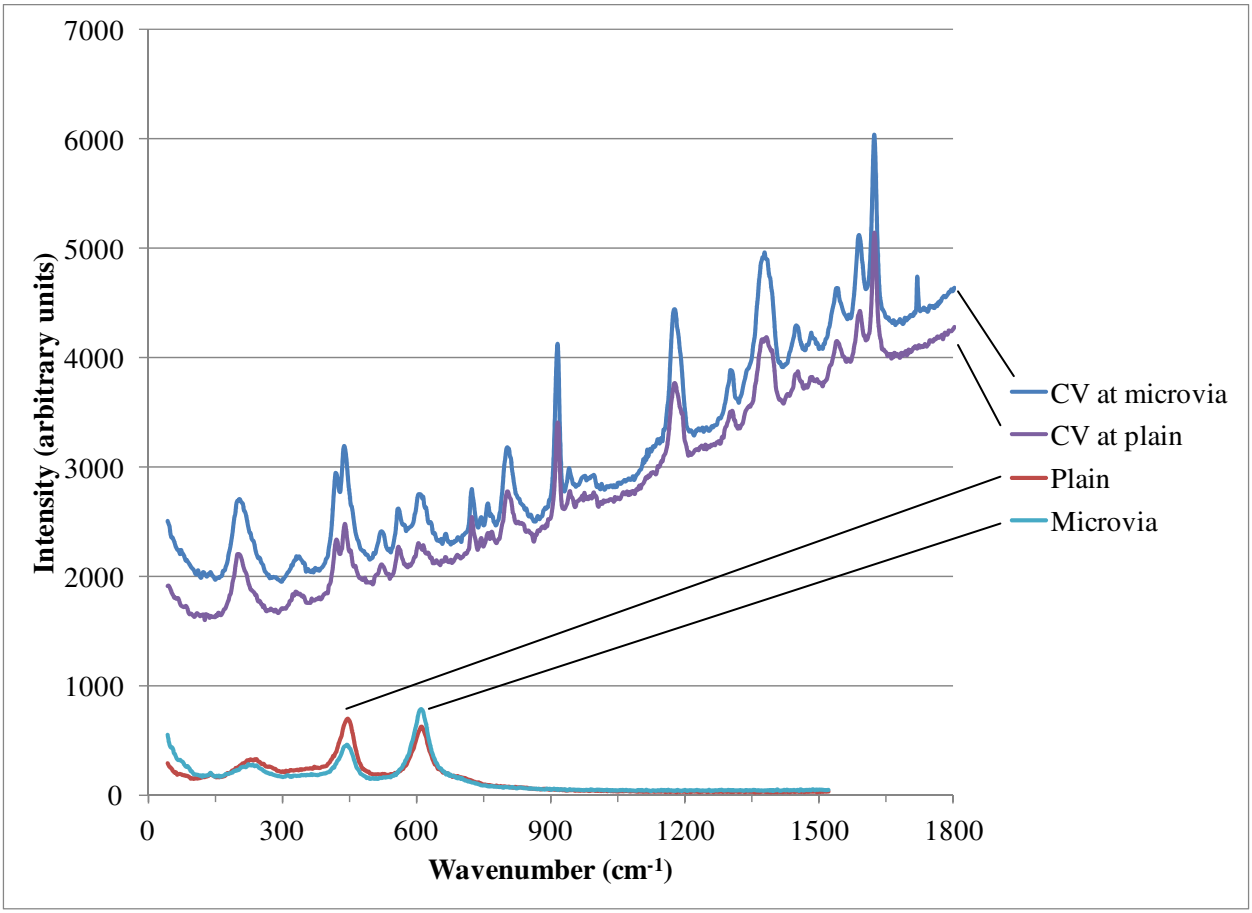

Figure A.3.6. CV-TiO_2 experiments using the 26 MHz -15msec substrate

The variations in 3-D nanofibrous porosity, TiO_2 phase composition impurities, crystallinity, nanofiber particle size averages and standard deviations as well as microvia morphology and network depth are all tunable with the femtosecond laser manufacturing technique. Investigating these factors the most is meaningful when developing a sensor for industrial use. The issue is that proving an enhancement for a CV dye may not be applicable, for instance, to aromatic pollutants with much lower Raman cross-sections and different adsorption kinetics. Therefore, it

is reasonable to conclude that the 3-D nanofiber network clearly has a significant potential to compete with the most popular Ag and Au substrates which will be subject to future research.

A.4 RAMAN ENHANCEMENT FACTOR CALCULATION

The Raman Enhancement Factor (EF) is typically determined with EM simulations by using generalized Mie theory (GMT)[111][83] and Finite Difference Time Domain techniques such as 2D-FDTD[89] and 3D-FDTD.[76] [112] However, these techniques are computationally limited to simple geometric systems such two-nanoparticle clusters of perfect spheres. In the present case, it is more appropriate to analyze the 3-D nanofibrous network structure experimentally. The following Raman EF equation is the most accepted in literature:[113]

$$\mathrm{EF}_{\mathrm{SERS}} = \frac{I_{\mathrm{SERS}}/N_{\mathrm{surf}}}{I_{\mathrm{ref}}/N_{\mathrm{bulk}}} \qquad \text{Eq. A.4.1}$$

where I_{SERS} represents the Raman SERS intensity, I_{ref} represents the Raman intensity without the TiO_2 nanofibrous substrate, N_{bulk} represents the number of molecules present under the confocal volume and N_{surf} represents the number of molecules responsible for the SERS response.

From Figure 6.1, $I_{SERS} = 6039$ and $I_{ref} = 113$ at 1623 cm^{-1} (shifted from 1621 cm^{-1}). The 1621 cm^{-1} wavenumber is the strongest CV vibrational mode which is used in such EF calculations.[114] The following equation is used to calculate N_{bulk}:

$$N_{\mathrm{bulk}} = \pi r^2 hcN_{\mathrm{A}} \qquad \text{Eq. A.4.2}$$

where, r represents the Raman laser spot radius (1.5 μm), h represents half the Depth of Field (DOF) of a tightly focused Raman laser (10/2 μm), c represents the Crystal Violet applied concentration (8.1×10^{-3} M) and N_A is the Avogadro constant. Following Eq. A.4.2, N_{bulk} is calculated to be 1.7×10^8 molecules. To calculate N_{surf}, knowledge of the nanofibrous surface area and CV adsorption to rutile TiO_2 are necessary. Surface area is expected to be similar to

electrospun TiO_2 nanowires as summarized by Table A.4.1. From Table A.4.1, the most conservative estimate of the most relevant architecture and phase is 2 m^2/g.

Table A.4.1. TiO_2 nanowires compared to the present study nanofibers

Author	Architecture †	Size (nm)	Phase	BET* (m^2/g)
present study	ds nanofiber	82+/-68	rutile	ca. 2.0
(Alves et al. 2009)[115]	dr	203+/-122	rutile	2.0
(Chuangchote et al. 2009)[116]	cr	264+/-86	mostly rutile	56
(Wang et al. 2011)[117]	dr	250+/-50	R/A = 0.61-2.43	32+/-8
(Hristovski et al. 2008)[118]	ds	65+/-35	anatase and rutile	126
(Doh et al. 2007)[119]	ds	194+/-71	anatase	26
(Madhugiri et al. 2004)[120]	ds	650+/-50	anatase	32
(Ray and Lalman 2011)[121]	cs	39+/-7	anatase	259+/-23

† d, discontinuous; c, continuous; s, smooth; r, rough.

*Brunauer–Emmett–Teller surface area model.

To determine the actual surface area within the laser sampling volume, it is necessary to determine the mass of TiO_2 within that region. Similarity relationships are used since it is not practical to weigh cubic micrometer volumes. Firstly, the mass of a rutile crystal is determined that would fit within the Raman sampling volume (Eq. A.4.3).

$$m_1 = \pi r^2 h \rho \qquad \text{Eq. A.4.3}$$

Rutile density ρ is 4.249 g/cm^3.[122] The new surface area SA_2 is then determined by using the BET surface area from Table A.4.1. By geometric similarity, the effective rutile TiO_2 nanofiber mass that is within the Raman sampling volume is determined by Eq. A.4.4.

$$m_2 = m_1 / \left(1 - \frac{SA_1 - SA_2}{2\pi r h}\right) \quad \text{Eq. A.4.4}$$

Therefore, by using the mass result of Eq. A.4.4 again with the BET surface area, the effective rutile TiO_2 nanofiber surface area within the Raman sampling volume is $SA_{eff} = 5.0x10^{-11}$ m^2. For N_{surf}, it is also necessary to determine the adsorption concentration of the CV dye to rutile TiO_2. Table A.4.2 summarizes the literature review for CV adsorption on TiO_2.

Table A.4.2. CV to TiO_2 adsorption equilibrium from UV-vis spectrophotometer measurements

Pertinence-Author	Interface, crystal or amorphous†	Adsorption (M)	Time (min)
present study	R, crystal	$2.9x10^{-6}$	ca. 1
(Hachem et al. 2001)[123]	Degussa P25, R/A=0.429, crystal	$2.9x10^{-6}$	45 - 90
(Kanna et al. 2010)[124]	Degussa P25, R/A=0.250, crystal	$2.5x10^{-5}$	30
(Dong et al. 2012)[125]	Degussa P25, crystal	$5.0x10^{-8}$	15
(Senthilkumaar and Porkodi 2005)[126]	A, crystal	$1.9x10^{-6}$	60
(Senthilkumaar and Porkodi 2005)[126]	A, crystal	$1.0x10^{-5}$	60
(Kanna et al. 2010)[124]	A, amorphous	$1.0x10^{-4}$	30

† R, rutile; A, anatase

Firstly, no CV dye adsorption on pure rutile data was found. In part, this has to do with the difficulty of synthesizing rutile. The most relevant studies used Degussa P25 that has a mix of both phases. Secondly, Senthilkumaar and Porkodi demonstrated that surface adsorption reduces significantly with increasing CV concentration (the concentration used in the present study was nearly 100 times greater). Thirdly, the SERS experiments were carried out immediately after CV

dye application, whereas adsorption equilibrium is expected to take at least 15 min (Table A.4.2). Therefore, the most conservative estimate of surface adsorption is to use c_{ads} = 2.9x10^{-6} M. Eq. A.4.5 represents the number of CV molecules adsorbed to the TiO_2 nanofibrous network.

$$N_{\text{surf}} = \text{SA}_{\text{eff}} \left(c_{\text{ads}} N_{\text{A}} \frac{1000\ L}{1\ m^3} \right)^{\frac{2}{3}} \qquad \text{Eq. A.4.5}$$

Substituting the variables and matching the parameter dimensions, N_{surf} = 7.2x10^3 molecules. Finally, inserting all the values back into Eq. A.4.1, the TiO_2 enhancement factor is calculated to be EF_{SERS} = 1.3x10^6. At this point, it should be noted that there are many sources of error when applying Eq. A.4.1 to determine the analytical Raman EF (Table A.4.3).

Table A.4.3. Sources of error when calculating the analytical Raman EF

Easier to Standardize	Harder to Standardize
dye /wavenumber used for calculation	laser tweezers effect on local concentration
laser focusing accuracy and precision	adsorption factor
time for adsorption equilibrium	variations in surface area after dye application
anatase to rutile TiO_2 ratio and crystallinity	effect of fluorescence
the exact concentration of the dye	

Table A.4.3 suggests that it is challenging to calculate an exact experimental Raman enhancement factor. Nonetheless, even the most conservative estimate of the nanofibrous TiO_2 3-D network implies an appreciable 10^6 order enhancement. This is already a major result given that only Ag and Au were previously thought to achieve such EM and charge transfer activity.

A.5 DETERMINING THE BEST RAMAN SENSOR PAD

Figure A.5.1 represents a relationship G = Sa – Sa / Max. This ties the average surface reflection roughness with the maximum reflection intensity. Since Sa « Max, the formula becomes more sensitive towards stable variations in Sa. The average is less susceptible to experimental error than the maximum PMT voltage. Since f : Sa → Max, it may be shown that Max → 0, G → -1. In other words, G = -1 is a perfectly reflection smooth surface and becomes rougher as G increases. It is also important to note that G is a formula construct as it is not dimensionally homogeneous. Such constructs are common in fluid mechanics (e.g. relating specific gravity S of an oil to its density in degrees API) and also for determining Brinell hardness of a metal.

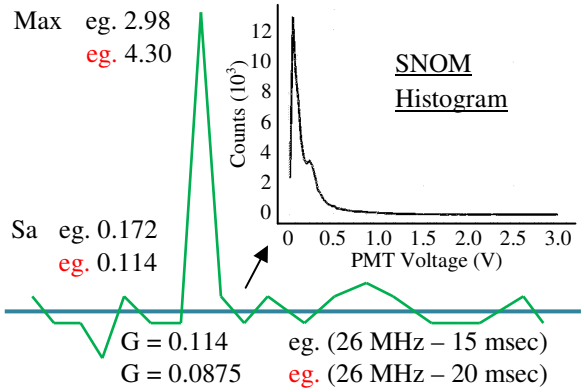

Figure A.5.1. Representation of G, where Sa (V) is the scan average reflection roughness and Max (V) is the maximum reflection per scan of Figure A.2.3

The G criterion is then used to plot Figure A.5.2. It is found that most of the SERS active nanofibrous TiO_2 sensor pads fit within the -0.0021 < G < +0.0411 band. There were only two exceptions marked by black stars at 4MHz – 25msec (G = -0.0171) and 26 MHz – 15 msec (G = 0.1145). Together with data outliers, there is still 90% confidence that the results are valid. The

extrapolation of this criterion to the rest of SNOM experiments is shown on the right of Figure A.5.2.

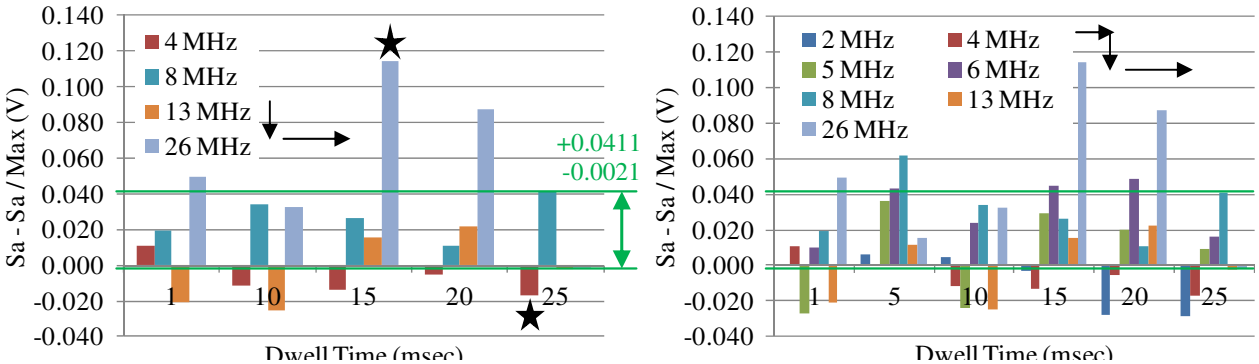

Figure A.5.2. Limits of Raman detection correlated with SNOM experiments (left: direct comparison to Raman, right: extrapolated results for the remainder of SNOM experiments, legend read left to right, the arrows indicate reading direction)

Figure A.5.3 reveals a logarithmic type of relationship between the G construct and the maximum PMT voltage. The two black points at 4 MHz – 5 msec and 2 MHz – 1 msec were determined to be outliers. Firstly, surface roughness at 2 MHz – 1 msec was Sa = 0.307 V (7x greater than other values at 2 MHz). For 4 MHz – 5 msec, Sa = 0.265 V (9x greater than other values at 4 MHz). Secondly, 4 MHz – 5 msec exceeds the maximum possible smoothness for Ti at G = -0.123. Removing the two outliers improves the logarithmic correlation by almost 20% (see the Raman Molecular Detection).

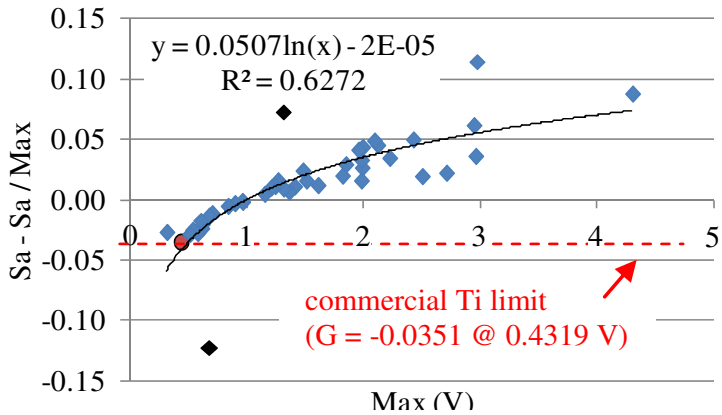

Figure A.5.3. Identified SNOM data outliers (black diamonds), R^2 correlation and curve of best fit reflects outlier inclusion

Irradiation laser fluence was considered to investigate the TiO_2 network synthesis parameters. The left side of Figure A.5.4 defines the threshold fluence reduction by the incubation principle after Jee, et al. (1988) and is represented as $\phi_{th}(n) = \phi_{th}(1)(tf)^{S-1}$,[49] where t is the irradiation dwell time (sec), f is the laser repetition rate (Hz), $\phi_{th}(1)$ is the threshold ablation fluence with one pulse (0.28 ± 0.02 J/cm^2 for Ti) and S is the incubation coefficient (0.83 ± 0.03 for Ti).[50] The right side of Figure A.5.4 defines the average fluence per target area $\phi_o = 4P / \pi f \omega_o^2$ where P is the average femtosecond laser power (16 W) and ω_o is the theoretical spot size diameter (m). The theoretical spot size diameter is represented as $\omega_o = 2\lambda F / \pi \omega_b$, where λ is the laser wavelength (515 nm), F is the effective telecentric lens focal length (12.478 mm) and ω_b is the beam waist diameter (8 mm).

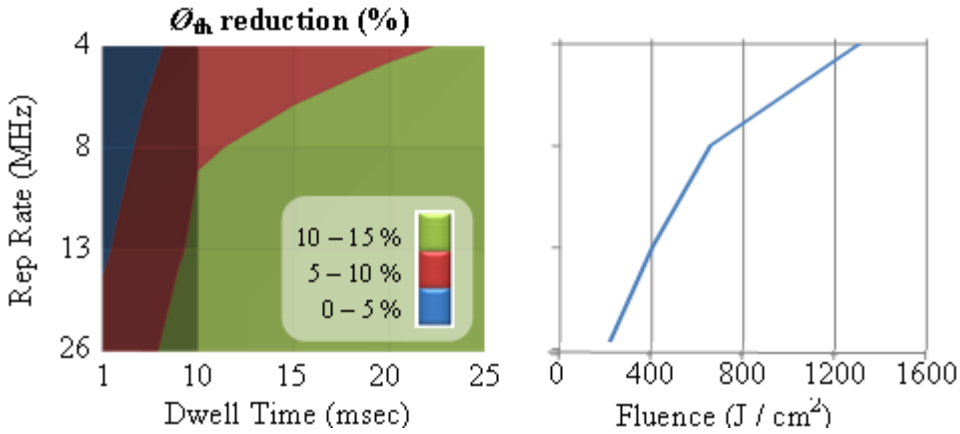

Figure A.5.4. Multiple-pulse femtosecond laser fluence characteristics with varying synthesis parameters

Earlier, a hypothesis that roughness plays a critical role in Raman analyte detection was presented (Figure A.5.3). Figure A.5.4 attempts to describe the phenomenon through synthesis parameters. It is shown that multiple pulse laser irradiation reduces the ablation fluence by up to 15%. Meanwhile, the laser fluence is reducing with increasing laser repetition rate. Consequently, the intermediate red band of Figure A.5.4 coincides with the null enhancement region of Figure 6.4.

A.6 CROSS-SECTION ANALYSIS

Since the TiO_2 nanofibers were mobile with respect to the AFM scanning probe, it was possible to scan the cross-section view of the microvias (Figure A.6.1).The flat lines at 0 μm are saturated responces from the AFM scanning head since the maximum scanning depth was limited to ca. 5 μm. The depth can be controlled by reducing the synthesis laser repetition rate and dwell time (Figure 4.1). The microvia depth is expected to have a positive correlation with the depth of the nanofiber network. However, SEM cross sections showing the nanofibers proved to be much more difficult.

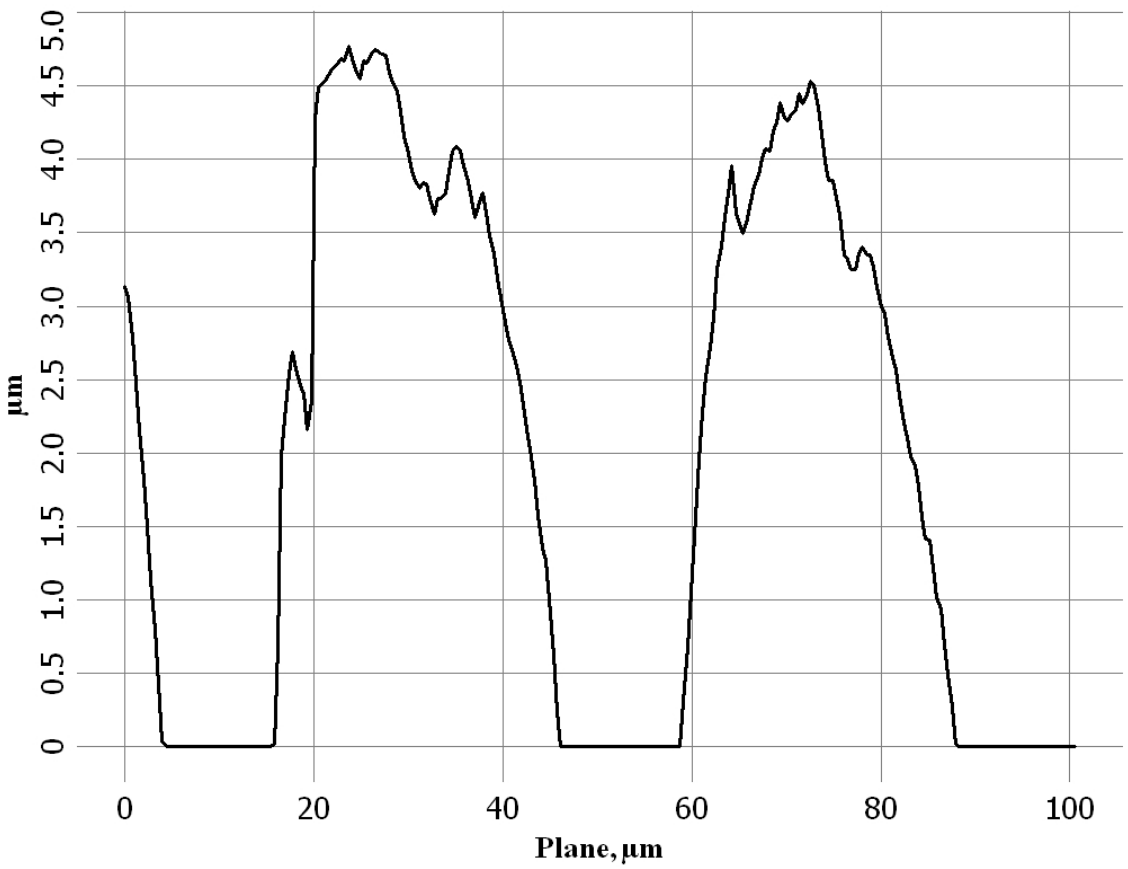

Figure A.6.1. AFM cross-sectional view of the top left substrate in Figure 4.7 (first cross section from the bottom of the AFM scan)

Titanium is a cumbersome material to machine. The commercial Ti sample used was 0.75 in thick. Various methods were attempted at cutting a cross section. Mechanical material removal processes such as sawing were not capable at cutting through the thickness. As a result, only diamond blade grinding could be used. The problem is that liquid coolant is required which inevitably washes away the nanofibers. Another method was considered to irradiate the sample on the edge. There were two major problems with this technique. Firstly, the heat dissipation is different resulting in plasma dynamics different from a standard surface. Second, there were significant safety concerns as the laser can scatter off the edge of the Ti sample and potentially

damage laboratory equipment and cause harm to the operators. Ti foil was used to alleviate the thickness problem. However, the intense heat from laser irradiation during synthesis heavily warped the foil. As a result, the surface did not have a consistent laser focus and could not generate the TiO_2 nanofiber network.

Nonetheless, we were previously able to make cross sectional views on silicon. Polished silicon wafers of 550 μm thickness were brittle and thin enough such that normal scribe and break methods resulted in reasonable SEM images. A cross section of Si nanofibers within the microvias was previously presented by Tavangar et al., 2010.[127] A cross section of a more developed nanofibrous 3-D network was presented by Sivakumar et al., 2010.[12] It is expected that the nanofibrous network will appear similar to the later work as it appears similar to TiO_2 nanofibrous networks from plan view.

REFERENCE LIST

[1] Ohsaka T., Izumi F., Fujiki Y., Raman spectrum of anatase, TiO2, *J. Raman Spectrosc*. 7, (1978) 321-324.

[2] Meagher E.P., Lager G.A., Polyhedral thermal expansion in the TiO2 polymorphs: refinement of the crystal structures of Rutile and Brookite at high temperature, *Can. Mineral*. 17 (1979) 77-85.

[3] Nomura-K. "Crystal Structure Gallery," 3. Elements, Compounds, Minerals, etc. (2002), http://staff.aist.go.jp/nomura-k/english/itscgallary-e.htm.

[4] Aitken R., Creely K., Tran C., Nanoparticles: An occupational hygiene review. Research Report, Health and Safety Executive (ed.), Institute of Occupational Medicine. HSE Books: London. 274 (2004).

[5] Chen Q., and Peng M., Structure and applications of titanate and related nanostructures, *Int. J. Nanotechnology* 4 (2007) 44-65.

[6] Ma R., Fukuda K., Sasaki T., Osada M., Bando Y., Structural features of titanate nanotubes/nanobelts revealed by Raman, X-ray absorption fine structure and electron diffraction characterizations, *J. Phys. Chem. B* 109 (2005) 6210-6214.

[7] Sun X. and Li Y., Synthesis and Characterization of Ion-Exchangeable Titanate Nanotubes, *Chem. Eur. J*. 9 (2003) 2229-2238.

[8] Michailowski A., AlMawlawi D., Cheng G., Moskovits M., Highly regular anatase nanotube arrays fabricated in porous anodic templates, *Chem. Phys. Lett*. 349 (2001) 1-5.

[9] Mor G., Varghese O., Paulose M., Shankar K., Grimes C., Visible light photoelectrochemical and water-photoelectrolysis properties of titania nanotube arrays, *Solar Energy Mat. & Solar Cells* 90 (2006) 2011-2075.

[10] Kim I., Rothschild A., Lee B., Kim D., Jo S., Tuller H., Ultrasensitive chemiresistors based on electrospun TiO2 nanofibers, *Nano Lett*. 6 (2006) 2009-2013.

[11] Tan B., Panchatsharam S., Venkatakrishnan K., High repetition rate femtosecond laser forming sub-10 μm diameter interconnection vias *J. Phys. D: Appl. Phys*. 42 (2009) 065102.

[12] Sivakumar M., Venkatakrishnan, K., Tan B., Study of metallic fibrous nanoparticle aggregate produced using femtosecond laser radiation under ambient conditions, *Nanotech*. 21 (2010) 225601.

[13] Tavangar A., Tan B., Venkatakrishnan K., Synthesis of bio-functionalized three-dimensional titania nanofibrous structures using femtosecond laser ablation, *Acta Biomaterialia* 7 (2011) 2726-2732.

[14] Kiani A., Venkatakrishnan K., Tan B., Direct patterning of silicon oxide on Si-substrate induced by femtosecond laser, *Opt. Express* 18 (2010) 1872.

[15] Luo X., Morrin A., Killard A., Smyth M., Application of nanoparticles in electrochemical sensors and biosensors, *Electroanal*. 4 (2005) 319-326.

[16] Ardo S. and Meyer G., Photodriven heterogeneous charge transfer with transition-metal compounds anchored to TiO2 semiconductor surfaces, *Chem. Soc. Rev*. 38 (2008) 115-164.

[17] Cosnier S., Senillou A., Gratzel M., Comte P., Vlachopoulos N., Renault N., Martelet C., Biomolecule immobilization on electrode surfaces by entrapment or attachment to electrochemically polymerized films. A review, *J. Electroanal. Chem*. 496 (1999) 176-181.

[18] Savage N., Akbar S., Dutta P., Titanium dioxide based high temperature carbon monoxide selective sensor, *Sensors and Actuators B* 72 (2001) 239-248.

[19] Varghese O., Gong D., Paulose M., Ong K., Grimes C., Hydrogen sensing using titania nanotubes, *Sensors and Actuators B* 93 (2003) 338-344.

[20] Volkmer A., Cheng J., Xie X., Theoretical and experimental characterization of coherent anti-Stokes Raman scattering microscopy, *Phys. Rev. Lett.* 87 (2001) 0239011-0239014.

[21] McGoverin C., Rades T., Gordon K., Recent pharmaceutical applications of Raman and terahertz spectroscopies *J. Pharm. Sci.* 97 (2008) 4598-4621.

[22] Zhang X., Young M.A., Lyandres O., Van Duyne R.P., Rapid detection of an anthrax biomarker by surface-enhanced Raman spectroscopy, *J. Am. Chem. Soc*. 127 (2005) 4484-4489.

[23] Wang Z., Zong S., Yang J., Song C., Li J., Cui Y., One-step functionalized gold nanorods as intracellular probe with improved SERS performance and reduced cytotoxicity, *Biosens. Bioelectron*. 26 (2010) 241-247.

[24] Tong L., Righini M., Gonzalez M.U., Quidant R., Käll M., Optical aggregation of metal nanoparticles in a microfluidic channel for surface-enhanced Raman scattering analysis, *Lab Chip* 9 (2009) 193-195.

[25] Huh Y.S., Erickson D., Aptamer based surface enhanced Raman scattering detection of vasopressin using multilayer nanotube arrays, *Biosens. Bioelectron*. 25 (2010) 1240-1243.

[26] Albrektsson T., Branemark P.I., Hansson H.A., Lindstrom, J., Osseointegrated titanium implants, *Acta Orthopaedica Scandinavica* 52 (1981) 155-170.

[27] Lee S., Kim S., Choo J., Soon Y.S., Lee Y.H., Ha Y.C., Ha S., Kang K., Chil H.O., Biological imaging of HEK293 cells expressing PLCγ1 using surface-enhanced Raman microscopy, *Anal. Chem*. 79 (2007) 916-922.

[28] Büchel D., Mihalcea C., Fukaya T., Atoda N., Tominaga J., Kikukawa T., Fuji, H., Sputtered silver oxide layers for surface-enhanced Raman spectroscopy, *App. Phys. Lett*. 79 (2001) 620-622.

[29] Vittadini A., Selloni A., Rotzinger F.P., Grätzel, M., Structure and Energetics of Water Adsorbed at TiO_ 2 Anatase 101 and 001 Surfaces, *Phys. Rev. Lett*. 81 (1998) 2954-2957.

[30] Ellingsen J.E., A study on the mechanism of protein adsorption to TiO2, *Biomater*. 12 (1991) 593-596.

[31] Li B., Franking R., Landis E.C., Kim H., Hamers, R.J., Photochemical grafting and patterning of biomolecular layers onto TiO2 thin films, *ACS Appl. Mater. Interfaces* 1 (2009) 1013-1022.

[32] Haynes C.L., McFarland A.D., Van Duyne R.P., Surface-enhanced Raman spectroscopy, *Anal. Chem*. 77 (2005) 338A-346A.

[33] Kittel C., Introduction to Solid State Physics, 7th Ed. Wiley, Singapore (1996).

[34] Arora A., Rajalakshmi M., Ravindran R., Phonon Confinement in Nanostructured Materials. Ed. Nalwa H. Encyclopedia of Nanosci. and Nanotech. Vol. X. American Scientific Publishers. Kalpakkam, (2003) pp.1-13.

[35] Yoon H.C., Kim H.-S., Functionalization of a poly (amidoamine) dendrimer with ferrocenyls and its application to the construction of a reagentless enzyme electrode, *Anal. Chem*. 2000 (72) 922-926.

[36] Nishida K., Morisawa K., Hiraki A., Muraishi S., Katoda T., In-Situ Monitoring of PE-CVD growth of TiO2 Films With Laser Raman Spectroscopy, *App. Surf. Sci*. 159-160 (2000) 143-148.

[37] Beattie I. and Gilson, T., Single Crystal Laser Raman Spectroscopy, *Proceeding of Royal Soc. A* 307 (1968) 407-429.

[38] Porto S.P.S., Fleury P.A., Damen T.C., Raman spectra of TiO2, MgF2, ZnF2, FeF2, and MnF2, *Phys. Rev*. 154 (1967) 522-526.

[39] Dayal B. The vibration spectrum of Rutile. In *Proceedings of the Indian Academy of Sciences - Section A*, Bangalore, India, (1950) p. 304.

[40] Mattsson A. and Osterlund, L., Adsorption and Photoinduced Decomposition of Acetone and Acetic Acid on Anatase, Brookite, and Rutile TiO2 Nanoparticles, *J. Phys. Chem. C* 114 (2010) 14121-14132.

[41] Balachandran U. and Eror N., Raman Spectra of Titanium Dioxide, *J. Solid State Chem*. 42 (1982) 276-282.

[42] Katiyar R. and Krishnan R., The vibration spectrum of Rutile, *Phys. Lett*. 12 (1967) 525-526.

[43] Narayanan P., Raman spectruim of Rutile (TiO2), *Indian Institute of Science* 48 (1950) 279-283.

[44] McDevitt N., Baun W., Infrared absorption study of metal oxides in the low frequency region (700-240cm^-1). *Spectrochimica Acta* 35 (1964) 799-808.

[45] Rietdorf J., *Special Optical Elements*. In Handbook of Biological Confocal Microscopy, New York, Springer Science-Business Media. LLC, (2006) pp. 43-58.

[46] Jariwala S., Venkatakrishnan K., Tan B., Single step self-enclosed fluidic channels via two photon absorption (TPA) polymerization, *Opt. Expess* 18 (2010) 1630-1636.

[47] Trager F., Handbook of Lasers and Optics. New York, New York (2007).

[48] Limpert J., Schreiber T., Clausnitzer T., Zollner K., Fuchs H., Kley E., Zellmer H., Tunnermann A., High-power femtosecond Yb-doped fiber amplifier, *Opt. Express* 10 (2002) 628-638.

[49] Jee Y., Becker M.F., Walser R.M., Laser-induced damage on single-crystal metal surfaces, *J. Opt. Soc. Am. B* 5 (1988) 648–659.

[50] Mannion P.T., Magee J., Coyne E., O'Connor G.M., Glynn T.J., The effect of damage accumulation behaviour on ablation thresholds and damage morphology in ultrafast laser micro-machining of common metals in air, *Appl. Surf. Sci*. 233 (2004) 275-287.

[51] Nazeeruddin M. K., Kay A., Rodicio I., Humphry-Baker R., Mueller E., Liska P., Vlachopoulos N., Graetzel M., Conversion of light to electricity by cis-X2bis (2, 2'-bipyridyl-4, 4'-dicarboxylate) ruthenium (II) charge-transfer sensitizers (X= Cl-, Br-, I-, CN-, and SCN-), *J. Am. Chem. Soc*. 115 (1993) 6382-6390.

[52] Moskovits M., DiLella D.P., Enhanced Raman spectra of ethylene and propylene adsorbed on silver, *J. Chem. Phys*. 73 (1980) 6068-6075.

[53] Gauthier M.A., Stangel I., Ellis T.H., Zhu X.X., A new method for quantifying the intensity of the C= C band of dimethacrylate dental monomers in their FTIR and Raman spectra, *Biomater*. 26 (2005) 6440-6448.

[54] Maher R.C., Hou J., Cohen L.F., Le Ru E.C., Hadfield J.M., Harvey J.E., Etchegoin P.G., Liu F.M., Green M.c, Brown R.J.C., Milton M.J.T., Resonance contributions to anti-

Stokes/Stokes ratios under surface enhanced Raman scattering conditions, *J. Chem. Phys*. 123 (2005) 084702.

[55] Song C., Wang Z., Zhang R., Yang J., Tan X., Cui Y., Highly sensitive immunoassay based on Raman reporter-labeled immuno-Au aggregates and SERS-active immune substrate, *Biosens. Bioelectron*. 25 (2009) 826-831.

[56] Zhang, X.; Young, M.; Lyandres, O.; Van Duyne, R.P. Rapid detection of an anthrax biomaker by surface-enhanced Raman spectroscopy. *J. Am. Chem. Soc*. 127 (2005) 4484.

[57] Chichkov B., Femtosecond, picosecond and nanosecond laser ablation of solids, App. Phys. 36 (1996) 109-115.

[58] ORegan B., Gratzel M., A low-cost, high-efficiency solar cell based on dye-sensitized colloidal Ti02 films, *Nature* 353 (1991) 737-740.

[59] Kasuga T., Hiramatsu M., Hoson A., Sekino T., Niihara K., Formation of titanium oxide nanotube, *Langmuir* 14 (1998) 3160-3163.

[60] Joo J., Kwon S., Yu T., Cho M., Lee J., Yoon J., Hyeon T., Large-Scale Synthesis of TiO2 Nanorods via Nonhydrolytic Sol-Gel Ester Elimination Reaction and Their Application to Photocatalytic Inactivation of E. coli, *J. Phys. Chem. B* 109 (2005) 15297-15302.

[61] Tarakeshwar P., Finkelstein-Shapiro D., Hurst S.J., Rajh T., Mujica V., Surface-Enhanced Raman Scattering on Semiconducting Oxide Nanoparticles: Oxide Nature, Size, Solvent, and pH Effects, *J. Phys. Chem. C* 115 (2011) 8994-9004.

[62] Konig J., Plasma evolution during metal ablation with ultrashort laser pulses, *Opt. Express* 91 (2005) 1-11.

[63] Stiles, P.L.; Dieringer, J.A.; Shah, N.C.; Van Duyne, R.P. Surface-enhanced Raman spectroscopy. *Annu. Rev. Anal. Chem*. 1 (2008) 601.

[64] Thoreson D., Liu Z., Chettiar K., Nyga P., Kildishev V., Drachev P., Shalaev M., *SANDIA Rep.* 2010 (2010) 3.

[65] Brown, R.J.C. and Milton, M.J.T. Nanostructures and nanostructured substrates for surface-enhanced Raman scattering (SERS). *J. Raman Spectrosc*. 39 (2008) 1313.

[66] Li S., Pedano L., Chang S., Mirkin A., Schatz C., Multi-functional crosslinked Au nanoaggregates for the amplified optical DNA detection, *Nano Lett*. 10 (2010) 1722.

[67] Kneipp J., Li X., Sherwood M., Panne U., Kneipp H., Stockman M.I., Kneipp K., Gold nanolenses generated by laser ablation-efficient enhancing structure for surface enhanced Raman scattering analytics and sensing, *Anal. Chem*. 80 (2008) 4247.

[68] Felidj N., Aubard J., Levi G., Krenn R., Hohenau A., Schider G., Leitner A., Aussenegg R., Optimized surface-enhanced Raman scattering on gold nanoparticle arrays, *Appl. Phys. Lett*. 82 (2003) 3095.

[69] Han Y., Liang Z., Sun H., Xiao H., Tsai L., Nanostructured substrate with nanoparticles fabricated by femtosecond laser for surface-enhanced Raman scattering, *Appl. Phys. A*. 102 (2011) 415-419.

[70] Jung D., Lee M., Lee Y., Kim H., Kim K., Lee K., Facile fabrication of large area nanostructures for efficient surface-enhanced Raman scattering, *J. Mater. Chem*. 16 (2006) 3145.

[71] Gutes A., Carraro C., Maboudian R., Silver nanodesert rose as a substrate for surface-enhanced Raman spectroscopy. Appl Mater Interfaces, *Appl. Mater. Interfaces*. 11 (2009) 2551.

[72] Choi J., Xu Z., Wu H., Liu L., Cunningham T., Surface-enhanced Raman nanodomes, *Nanotech*. 21 (2010) 415301.

[73] Lombardi J.R., Birke R.L., A unified approach to surface-enhanced Raman spectroscopy, *J. Phys. Chem. C* 112 (2008) 5605-5617.

[74] Coluccio L., Das G., Mecarini F., Gentile F., Pujia A., Bava L., Tallerico R., Candeloro P., Liberale C., Angelis D., Fabrizio E.D., Silver-based surface enhanced Raman scattering (SERS) substrate fabrication using nanolithography and site selective electroless deposition, *Microelectron. Eng*. 86 (2009) 1085.

[75] Mo D. and Ching Y., Electronic and optical properties of three phases of titanium dioxide: rutile, anatase, and brookite, *Phys. Rev. B*. 51 (1995) 13023.

[76] Tian Z., Yang Z., Wu D., SERS From Transition Metals and Excited by Ultraviolet Light, in: Kneipp K., Moskovits M., Kneipp H. (Eds.), Topics in Appl. Phys., Springer, Berlin, (2006) pp. 125-146.

[77] Kelly L., Coronado E., Zhao L., Schatz C., The optical properties of metal nanoparticles: the influence of size, shape, and dielectric environment, *J. Phys. Chem. B*. 107 (2003) 668.

[78] Bhagavantam S. and Venkatarayudu T., In *Proceedings of the Indian Academy of Sciences - Section A*, Bangalore, India (1939) p. 224.

[79] Fleger Y. and Rosenbluh M., Controlling the optical spectra of gold nano-islands by changing the aspect ratio and the inter-island distance: theory and experiment, *Res. Lett. in Optics*. 2009 (2009) 1.

[80] Hwang J., Chen K., Hong S., Chen S., Syu W., Kuo C., Syu W., Lin Y., Chiang H., Chattioadhyay S., Chen K.H., Chen C., The preparation of silver nanoparticle decorated

silica nanowires on fused quartz as reusable versatile nanostructured surface-enhanced Raman scattering substrates, *Nanotech*. 21 (2010) 1.

[81] Jensen R., Duval L., Kelly L., Lazarides A., Schatz C., Van Duyne P., Nanosphere lithography: effect of the external dielectric medium on the surface plasmon resonance spectrum of a periodic array of silver nanoparticles, *J. Phys Chem*. B. 103 (1999) 9846.

[82] Suh D., Schenter K., Zhu L., Lu P., Probing nanoscale surface enhanced Raman-scattering fluctuation dynamics using correlated AFM and confocal ultramicroscopy, *Ultramicrosc*. 97 (2002) 89.

[83] Bidault S., Abajo G., Polman A., Plasmon-based nanolens assembled on a well-defined DNA template, *J. Am. Chem. Soc*. 130 (2008) 2750.

[84] Li J., Song S., Li D., Su Y., Huang Q., Zhao Y., Fan C., Multi-functional crosslinked Au nanoaggregates for the amplified optical DNA detection, *Biosens. Bioelectron*. 24 (2009) 3311.

[85] Mahmood A., Venkatakrishnan K., Tan B., Alubaidy, M.,Synthesis of Visible Light-Active Nanostructured TiO2 via Femtosecond Laser Irradiation in Air, *Int. J. Green Nanotech. Mat. Sci. Eng*. 2 (2010) M9-M14.

[86] Shoute T., Bergren J., Mahmoud M., Harris D., McCreery L., Optical interference effects in the design of substrates for surface-enhanced Raman spectroscopy, *Appl. Spectrosc*. 63 (2009) 133.

[87] Naoi K., Ohko Y., Tatsuma T., TiO2 films loaded with silver nanoparticles: control of multicolor photochromic behavior, *J. Am. Chem. Soc*. 126 (2004) 3664.

[88] Ye J., Shioi M., Lodewijks K., Lagae L., Kawamura T., Dorpe P.V., Tuning plasmonic interaction between gold nanorings and a gold film for surface enhanced Raman scattering, *Appl. Phys. Lett.* 97 (2010) 163106.

[89] Hatab A., Hsueh C., Gaddis L., Retterer T., Li J., Eres G., Zhang Z., Gu B., Free-standing optical gold bowtie nanoantenna with variable gap size for enhanced Raman spectroscopy, *Nano Lett*. 10, (2010) 4952.

[90] Kneipp K., Haka S., Kneipp H., Babizadegan K., Yoshizawa N., Boone C., Peltier S., Motz T., Dasari R., Feld S., . Surface-enhanced Raman spectroscopy in single living calls using gold nanoparticles, *Appl. Spectrosc*. 56 (2002) 150.

[91] Kneipp K., Wang Y., Kneipp H., Perelman T., Itzkan I., Single molecule detection using surface-enhanced Raman scattering (SERS), *Phys. Rev. Lett*. 78 (1997) 1667.

[92] Krishnan A.V., Stathis P., Permuth S.F., Tokes L., Feldman, D., Bisphenol-A: an estrogenic substance is released from polycarbonate flasks during autoclaving, *Endocrinology* 132 (1993) 2279-2286.

[93] Ye S., Morita S., Li G., Noda H., Tanaka M., Uosaki K., Osawa, M., Structural changes in poly (2-methoxyethyl acrylate) thin films induced by absorption of bisphenol A. An infrared and sum frequency generation (SFG) study, *Macromolecules* 36 (2003) 5694-5703.

[94] Deng A., Himmelsbach M., Zhu Q.-Z., Frey S, Sengl M., Buchberger W., Niessner R., Knopp, D., Residue analysis of the pharmaceutical diclofenac in different water types using ELISA and GC-MS, *Environ. Sci. Technol*. 37 (2003) 3422-3429.

[95] Canamares V., Chenal C., Birke L., Lombardi R., DFT, SERS, and single-molecule SERS of crystal violet, *J. Phys. Chem. C* 112 (2008) 20295.

[96] Musumeci A., Gosztola D., Schiller T., Dimitrijevic M., Mujica V., Martin D., Rajh T., SERS of Semiconducting Nanoparticles (TiO2 Hybrid Composites), *J. Am. Chem. Soc*. 131 (2009) 6040.

[97] Li G., Morita S., Ye S., Tanaka M., Osawa, M., Hydrogen bonding on the surface of poly (2-methoxyethyl acrylate), *Anal. Chem*. 76 (2004) 788-795.

[98] Kurt M., Yurdakul, S., Molecular structure and vibrational spectra of 1, 2-bis (4-pyridyl) ethane by density functional theory and ab initio Hartree-Fock calculations, *J. Mol. Struct*. 654 (2003) 1-9.

[99] Iliescu T., Baia M., Kiefer W., FT-Raman, surface-enhanced Raman spectroscopy and theoretical investigations of diclofenac sodium, *Chem. Phys*. 298 (2004) 167-174.

[100] Weerd J., Kazarian S., Release of poorly soluble drugs from HPMC tablets studied by FTIR imaging and flow-through dissolution tests, *J. Pharm. Sci*. 94 (2005) 2096-2109.

[101] Sheu M.-T., Chou H.-L., Kao C.-C., Liu C.-H., Sokoloski T.D., Dissolution of diclofenac sodium from matrix tablets, *Int. J. Pharm*. 85 (1992) 57-63.

[102] Liu G.-K., Ren, B., Wu D.-Y., Duan S., Li J.-F., Yao J.-L., Gu R.-A., Tian Z.-Q., Effect of intrinsic properties of metals on the adsorption behavior of molecules: Benzene adsorption on Pt group metals, *J. Phys. Chem. B* 11 (2006) 17498-17506.

[103] Wang C.-Y., Groenzin H., Shultz M.J., Surface characterization of nanoscale TiO2 film by sum frequency generation using methanol as a molecular probe, *J. Am. Chem. Soc.* 127 (2005) 9736-9744.

[104] Pettibone J.M., Cwiertny D.M., Scherer M., Grassian, V.H., Adsorption of organic acids on TiO2 nanoparticles: Effects of pH, nanoparticle size, and nanoparticle aggregation, *Langmuir* 24 (2008) 6659-6667.

[105] Mandal M., Jana N.R., Kundu S., Ghosh S.K., Panigrahi M., Pal T., Synthesis of Au core–Ag shell type bimetallic nanoparticles for single molecule detection in solution by SERS method, *J. Nanoparticle Res*. 6 (2004) 53-61.

[106] Baia M., Melinte G., Barbu-Tudoran L., Diamandescu L., Iancu V., Cosoveanu V., Danciu V., Baia L., Highly porous nanocomposites based on TiO2-noble metal particles for sensitive detection of water pollutants by SERS, *J. Phys.: Conference Series* 304 (2011) 012059.

[107] Panarin A.Yu., Terekhov S.N., Kholostov K.I., Bondarenko V.P., SERS-active substrates based on n-type porous silicon, *Appl. Surf. Sci*. 39 (2010) 123-138.

[108] Yang L., Jiang X., Ruan W., Zhao B., Xu W., Lombardi J.R., Observation of Enhanced Raman Scattering for Molecules Adsorbed on TiO2 Nanoparticles: Charge-Transfer Contribution, *J. Phys. Chem. C* 112 (2008) 20095-20098.

[109] Maruyama Y., Futamata M., Elastic scattering and emission correlated with single-molecule SERS, *J. Raman. Spectrosc*. 36 (2005) 581-592.

[110] McCreery R.L., Raman Spectroscopy for Chemical Analysis first vol. John Wiley & Sons, New York, New York (2000).

[111] Gopinath A., Boriskina S.V., Premasiri W.R., Ziegler L., Reinhard B.M., Negro L.D., Plasmonic nanogalaxies: multiscale aperiodic arrays for surface-enhanced Raman sensing, *Nano Lett*. 9 (2009) 3922.

[112] Dallapiccola R., Gopinath A., Stellacci F., Dal Negro L., Quasi-periodic distribution of plasmon modes in two-dimensional Fibonacci arrays of metal nanoparticles. *Opt. Express* 16 (2008) 5544-5555.

[113] Le Ru E., Blackie E., Meyer M., Etchegoin P., Surface Enhanced Raman Scattering Enhancement Factors: A Comprehensive Study, *J. Phys. Chem. C* 111 (2007) 13794-13803.

[114] Bechelany M., Brodard P., Philippe L., Michler J., Extended domains of organized nanorings of silver grains as surface-enhanced Raman scattering sensors for molecular detection, *Nanotech*. 20 (2009) 455302-455310.

[115] Alves A., Berutti F., Clemens F., Graule T., Bergmann C., Photocatalytic activity of titania fibers obtained by electrospinning, *Mat. Res. Bulletin* 44 (2009) 312-317.

[116] Chuangchote S., Jitputti J., Sagawa T., Yoshikawa S., Photocatalytic Activity for Hydrogen Evolution of Electrospun TiO2 Nanofibers, *App. Mat. Int.* 9 (2009) 1140-1143.

[117] Wang C., Zhang X., Shao C., Zhang Y., Yang J., Sun P., Liu X., Liu H., Liu Y., Xie T., Wang D., Rutile TiO2 nanowires on anatase TiO2 nanofibers: A branched heterostructured photocatalysts via interface-assisted fabrication approach, *J. Colloid Interface Sci.* 363 (2011) 157-164.

[118] Hristovski K., Westerhoff P., Crittenden J., An approach for evaluating nanomaterials for use as packed bed adsorber media: A case study of arsenate removal by titanate nanofibers, *J. Hazard. Mater.* 156 (2008) 604-611.

[119] Joo Doh S., Kim C., Geun Lee S., Jun Lee S., Kim H. Development of photocatalytic TiO2 nanofibers by electrospinning and its application to degradation of dye pollutants, *J. Hazard. Mater.* 154 (2008) 118-157.

[120] Madhugiri S., Sun B., Smirniotis P., Ferraris J., Balkus K., Electrospun mesoporous titanium dioxide fibers, *Microporous Mesoporous Mater.* 69 (2004) 77-83.

[121] Ray S., Lalmanb J., Using the Box–Benkhen design (BBD) to minimize the diameter of electrospun titanium dioxide nanofibers, *Chem. Eng. J.* 169, (2011) 116-125.

[122] Barnard A., Zapol P., Curtiss L., Modeling the Morphology and Phase Stability of TiO2 Nanocrystals in Water, *J. Chem. Theory Comput.* 1 (2005) 107-116.

[123] Hachem C., Bocquillon F., Zahraa O., Bouchy M., Decolourization of textile industry wastewater by the photocatalytic degradation process, *Dyes and Pigments* 49 (2001) 117–125.

[124] Kanna M., Wongnawa S., Buddee S., Dilokkhunakul K., Pinpithak P., Amorphous titanium dioxide: a recyclable dye remover for water treatment, *J. Sol-Gel Sci. Technol.* 53 (2010) 162-170.

[125] Dong W., Sun Y., Ma Q., Zhua L., Huac W., Lub X., Zhuanga G., Zhanga S., Guoa Z., Zhaoc D., Excellent photocatalytic degradation activities of ordered mesoporous anatase TiO2–SiO2 nanocomposites to various organic contaminants, *J. Hazard. Mater.* 229-230 (2012) 307-320.

[126] Senthilkumaar S. and Porkodi K., Heterogeneous photocatalytic decomposition of Crystal Violet in UV-illuminated sol–gel derived nanocrystalline TiO2 suspensions, *J. Colloid Interface Sci.* 288 (2005) 184–189.

[127] Tavangar A., Tan B., Venkatakrishnan K., Single-step fabrication of microfluidic channels filled with nanofibrous membrane using femtosecond laser irradiation, *J. Micromech. Microeng.* 20 (2010) 085016-085022.

CV

DMITRY MAZNICHENKO

dmitry.maznichenko@ryerson.ca

Education:

Ryerson University, Toronto, ON

MASc in Mechanical Engineering (2010-current)

Specialty: mfg., mater. and solid mechanics

CGPA: 4.33/4.33

BEng in Mechanical Engineering (2006-2010)

Specialty: mfg.

CGPA: 3.39/4.33

Selected Honors:

RU - SEB fellowship candidate	TBC
RU - nominee for best teacher assistant award	2011
RU - graduate award and student stipend	2010
American Foundry Society - Robert Taylor memorial schlr.	2010

Publications under review:

"Stimulating Multiple SERS Mechanisms from Titanium Dioxide (TiO_2) by a Nanofibrous 3-D Network Structure." D. Maznichenko, K. Venkatakrishnan, B. Tan. Langmuir, with revision.

"TiO_2 Nanofibrous Interface Development for Raman Detection of Environmental Pollutants." D. Maznichenko, R. Selvaganapathy, K. Venkatakrishnan, B. Tan App. Phys. Lett.